Molecular BioSystems

Accepted Manuscript

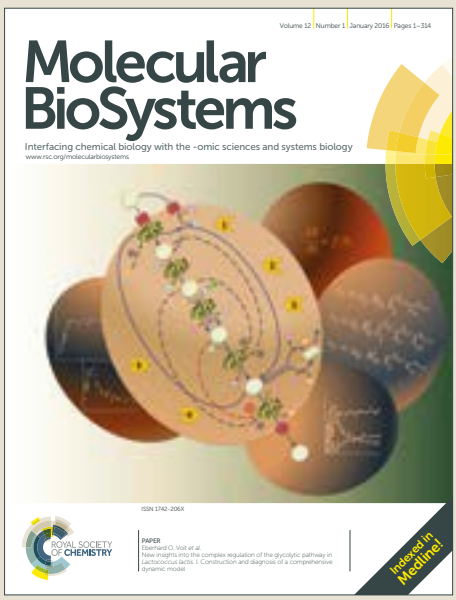

This is an Accepted Manuscript, which has been through the Royal Society of Chemistry peer review process and has been accepted for publication.

Accepted Manuscripts are published online shortly after acceptance, before technical editing, formatting and proof reading. Using this free service, authors can make their results available to the community, in citable form, before we publish the edited article. We will replace this Accepted Manuscript with the edited and formatted Advance Article as soon as it is available.

You can find more information about Accepted Manuscripts in the author guidelines.

Please note that technical editing may introduce minor changes to the text and/or graphics, which may alter content. The journal's standard Terms & Conditions and the ethical guidelines, outlined in our author and reviewer resource centre, still apply. In no event shall the Royal Society of Chemistry be held responsible for any errors or omissions in this Accepted Manuscript or any consequences arising from the use of any information it contains.

ROYAL SOCIETY OF CHEMISTRY

rsc.li/molecular-biosystems

Molecular Biosystems

Full Paper

Probing Oligomerization of Amyloid Beta Peptide in Silico

L. Dorosh[a,b] and M. Stepanova[a,b,c]†

Received 00th January 20xx,
Accepted 00th January 20xx

DOI: 10.1039/x0xx00000x

www.rsc.org/

Aggregation of amyloid β (Aβ) peptide is implicated in fatal Alzheimer's disease, for which no cure is available. Understanding of mechanisms responsible for the aggregation is required for therapies to be developed. In an effort to better understand molecular mechanisms involved in spontaneous aggregation of Aβ peptide, extensive molecular dynamics simulations are reported, and the results analyzed through a combination of structural biology tools and a novel essential collective dynamics method. Several model systems composed of ten or twelve Aβ17-42 chains in water are investigated, and the influence of metal ions is probed. The results suggest that Aβ monomers tend to aggregate into stable globular-like oligomers with 13% – 23% of β-sheet content. Two stages of the oligomer formation have been identified, quick collapse within the first 40 ns of the simulation characterized by a decrease of inter-chain separation and buildup of β-sheets, and subsequent slow relaxation of the oligomer structure. The resulting oligomers comprised a stable, coherently moving sub-aggregate of 6-9 strongly inter-correlated chains. Ions Cu^{2+} and Fe^{2+} have been found to develop coordination bonds with carboxylate groups of E22, D23 and A42, which remain stable during 200 ns simulations. The presence of Fe^{2+}, and particularly Cu^{2+} ions in negatively charged cavities has been found to cause significant changes in the structure and dynamics of the oligomers. The results indicate, in particular, that formation of non-fibrillar oligomers might be involved in early template-free aggregation of Aβ17-42 monomers, with charged species such as Cu^{2+} or Fe^{2+} ions playing an important role.

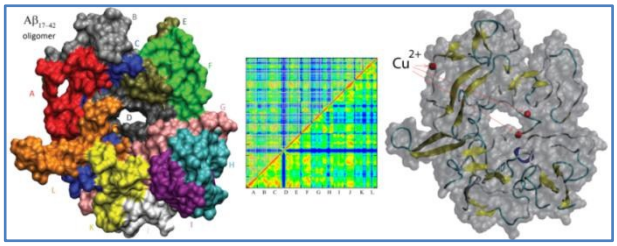

Introduction

The unique ability of proteins to adopt different conformations and to selectively and tightly bind other molecules determines their diverse functions, but the same ability can also cause protein's misfolding and aggregation. Toxic protein aggregates have been implicated in amyloidosis diseases, including Alzheimer's disease (AD), Parkinson's disease (PD), *amyotrophic lateral sclerosis* (ALS), and transmissible spongiform encephalopathies (TSE) [1,2]. Since the plaques and fibrils of amyloid β (Aβ) peptide were found in the brains of patients suffering from Alzheimer's disease, the amyloid (cascade) hypothesis emerged in early 90th stating that the Aβ peptide fibrils are responsible for the pathology of AD [3]. However, subsequently evidence was collected towards an alternative toxic oligomer hypothesis suggesting that smaller, soluble amyloid oligomers known as "seeds" or toxic pre-fibrillar aggregates, rather than mature plaques and fibrils, determine neurodegeneration in AD and other protein misfolding diseases [4–8]. For example, polyclonal antibodies were found to supress the toxicity of many soluble oligomers from different proteins (indicating common structural features), but they did not bind to mature fibrils [7]. Recent experimental studies indicate in particular that $A\beta_{42}$ oligomers,

[a] *Department of Electrical and Computer Engineering, University of Alberta; Edmonton, Alberta, Canada.*
[b] *National Research Council of Canada; Edmonton, Alberta, Canada;*
[c] *Department of Physics, Astronomy, and Materials Science, Missouri State University, Springfield, MO, USA.*
† Corresponding author
E-mail: ms1@ualberta.ca; mariastepanova@missouristate.edu
Current Address: Department of Electrical and Computer Engineering, University of Alberta; 11-203 Donadeo Innovation Centre for Engineering, 9211-116 Street NW, Edmonton, Alberta, Canada T6G 1H9. Phone: 1-780-492-3332
Electronic Supplementary Information (ESI) available: [details of any supplementary information available should be included here]. See DOI: 10.1039/x0xx00000x

rather than fibrils, bind to lipid membranes causing their damage [9]. Experiments on misfolded Aβ peptide, α-synuclein, and transthyretin also suggest that amyloidogenic cytotoxicity may share a common mechanism unrelated to the specific sequence [1]. Structure-based screening of compounds that bind to amyloid fibers (BAFs) allowed to find BAFs which decreased Aβ peptide toxicity but not its fibrillation propensity [10]. Another hypothesis suggests that plaques may play a role in trapping of toxic oligomers converting them into a more inert form [11,12]. This in turn suggests that a dynamic equilibrium may exist in transition state between the two species highlighting the importance of understanding detailed molecular mechanisms behind their interactions at various stages of aggregation.

Specifically for Aβ peptide, monomers are found in soluble form and largely unstructured, with partial α-helical [13] or β-strand [14] structure. They are believed to acquire β content when they aggregate [13]. The term oligomer is employed to describe many aggregated species, from low-molecular-weight (less than eight units) to high-molecular-weight species of various symmetries. The term protofibril usually denotes a β-sheet rich heterogeneous kinetic intermediate arising before a mature fibril structure is formed. Stable entities which serve as nuclei for aggregation when introduced in solution containing Aβ monomers are known as seeds [15].

Two types of Aβ peptide fragments known as P3 ($Aβ_{17-40/42}$) and P4 ($Aβ_{1-40/42}$) can be derived from amyloid precursor protein (APP) by two mutually exclusive proteolytic pathways via cleavage by α-/γ- and β-/γ-secretases, respectively [16]. These fragments are believed to form small and mobile neurotoxic oligomers. Other fragments, such as $Aβ_{1-16}$ or $Aβ_{25-35}$, have also been studied, however only P3 and P4 peptides have been associated with neuroinflammation [16]. Neurotoxic effects of P3 activated through a specific signal transduction pathway were also reported [17]. Although P3 was absent or sparse in aged non-AD brains, insoluble diffuse deposits of P3 were found in nervous and vesicular systems associated with AD pathology [18,19]. Diffuse non-fibrillar deposits consisting mainly of $Aβ_{17-42}$ were also found in the gray and white matter and leptomeningeal/cortical vessels of AD patients after vaccination against fibrillar $Aβ_{42}$ [20]. It was concluded that solubilized Aβ peptides from such deposits may ultimately have cascading toxic effects on cerebrovascular, gray and white matter tissues [20]. As a potential mechanism, membrane-destabilising properties of C-terminal domain of Aβ peptide have been hypothesized [21].

In the cerebrospinal fluid of non-demented controls about one-half of the Aβ end at amino acid 40, 16% end at amino acid 38, and 10% end at amino acid 42 [22]. Increased production rates of $Aβ_{42}$ in comparison to $Aβ_{40}$ have been found in AD patients, and therefore associated with AD synaptic changes [23]. Due to more exposed hydrophobic residues of $Aβ_{1-42}$, this construct tends to aggregate faster than Aβ1-40 [24]. Also, increased proportion $Aβ_{42}$:$Aβ_{40}$ has been shown to enhance synaptotoxicity [25]. $Aβ_{1-42}$ dimers, tetramers, hexamers, and dodecamers have been detected in ion mobility spectroscopy-MS in vitro experiments [26,27]. Multiples of $Aβ_{1-42}$ hexamers have also been observed [27,28]. Recent study of early stages of aggregation [29] suggests that monomeric $Aβ_{1-40}$ and $Aβ_{1-42}$ peptides tend to coalesce into largely unstructured globules from 15 nm in diameter, which slowly grow larger until a sharp transition occurs to nucleation and growth of β-rich fibrillar structures. Formation of the fibrils was found faster in $Aβ_{1-42}$ peptide than in $Aβ_{1-40}$ peptide. Cell toxicity tests have indicated that the most toxic species is formed at early stage of aggregation when unstructured globules are observed, leading to a hypothesis that the globules themselves represent the toxic species [29]. A very recent high-resolution atomic force microscopy study shows specifically that soluble oligomers $Aβ_{42}$, rather than $Aβ_{40}$, quickly become dominant oligomers with the propensity of seed and protofibrilar structures formation in aggregation experiments *in-vitro* [30]. Also, it has been demonstrated [31] that Aβ fragments 24-34, 25-35, and 26-36 alone may form oligomeric structures resembling cylindrins and β-barrels.

It is believed that toxic Aβ oligomers can interact with cell membranes, cause oxidative stress, and increase the amount of transition metal ions, which in turn may lead to cell death [7,32]. Since metal ions have been found in high concentrations in the senile plaque core and rim in AD brains [33–35], the Aβ and APP were even identified as Al/Cu/Zn/Fe metalloproteins. Three N-terminal histidine residues H6, H13, and H14, and tyrosine Y10 have been identified as main high-affinity Cu^{2+} coordinating residues [36–41]. However, deprotonated main-chain amide groups or carboxylate groups D1, E3, D7, E11, E22, and D23, as well as methionine M35 are also expected to play a role in transient coordination of metal ions [36–38,41]. Studies suggest that a large region involving N-terminal and adjacent area [36], might be involved in coordination of Cu^{2+} ions, whereas Zn^{2+} might interact with central region around residues 26-28 [39,42]. Experimental studies of possible role of metal ions in the aggregation are also in the pipeline. The metal chelation was shown to dissolve amyloid aggregates, therefore reversing Aβ aggregation [34]. Moreover, the rapid acceleration of Aβ oligomer aggregation dynamics was observed in experiments in the presence of Zn and Al, whereas Cu and Fe showed limited propensity for Aβ aggregation [33–35,43]. Cu and Zn prevented Aβ from forming fibrils [44], however Zn promoted formation of small globular aggregates, while Cu produced poorly-structured micro-aggregates [45]. However, a different group [46] found Cu inhibiting Aβ aggregation by competing with Zn for histidine residues.

Broader aspects of electrostatic, hydrophobic, and other non-covalent interactions on Aβ aggregation have been studied extensively [47–50]. Protofibril formation is believed to be driven by hydrophobic, aromatic and steric interactions, with fold 21-30 playing an important role. A strong evidence that aromatic interactions from the phenylalanine and tyrosine rings play important role in amyloid formation has been reported [51]. These interactions are complemented with electrostatic interactions, particularly hydrogen bond V21-K28 and salt bridge E22/23-K28. A recent four-dimensional electron microscopy study [52] indicates that forces responsible for amyloid stability are highly anisotropic, and that inter-

backbone hydrogen bonding network within β-sheets is 20 times more rigid than side-chain interactions.

Overall, the body of literature addressing Aβ peptide structure, aggregation, and the associated toxicity has increased exponentially for the last two decades, APP thereby becoming "the most studied protein in the 21st century" [53]. However, despite the significant progress, detailed mechanisms of toxic oligomers (seeds) formation, and their exact structure remain elusive. Complementary to the experimental studies, molecular dynamics (MD) simulations and other computational models provide important insights into detailed atomistic mechanisms of Aβ peptide misfolding, aggregation, and fibril growth [50,54–57]. Thus, many computational works study the structure and dynamics of Aβ peptide monomers [58–63] employing disordered amyloid peptide constructs and/or known NMR structures of insoluble fibril fragments as the initial structure models. Early stages of oligomerization were also investigated, particularly addressing dimers [62,64–66] and other small size oligomers [49,67–72]. Such computational studies allowed identifying the dock and lock mechanism of fibril formation, U-shape topology of β-sheet-turn-β-sheet motif of the peptide, clarified the role of water in aggregation, elucidated how Aβ peptide protofibrils might be solvated, and what may affect their stability. Recently, Aβ dodecamers have been constructed from monomers employing a docking algorithm, and their structural evolution of analyzed [73]. After 4 ns MD simulations, the dodecameric Aβ complexes have been found stable within hydrophobic core, albeit not entirely ordered [73]. The mechanisms of Aβ oligomers interaction with cell membranes are not obvious yet, however a role might be played by their ability to form membrane pores (ion channels). Simulations [74] have shown that $A\beta_{17-42}$ peptides indeed can form ion channels in lipid bilayer, and that these ion channels might be blocked by Zn^{2+} ions. Simulation studies also indicate [75] that binding of Zn^{2+} ions to individual Aβ peptide molecules may significantly change their conformational distribution. Binding of Cu^{2+} ions by monomeric Aβ peptide has been investigated by MD simulations as well [76]. The study suggests that binding of Cu^{2+} ions in the H13-H14 region of $A\beta_{1-42}$ in solution may be accompanied by coordination of the ions by carboxyl groups D1, E3, and E22 via electrostatic attraction.

Molecular dynamics sampling of conformational space for $A\beta_{1-42}$ peptide oligomers is computationally expensive. Especially all-atom simulations of Aβ multimers containing the flexible N-terminal region $A\beta_{1-16}$ would exhibit a substantially slower aggregation process in comparison to shorter chains [54], urging the development and application of various cost-reduction methods, or using shorter fragments of the peptide. Some works use coarse-grained models, such as the discrete MD with four bead peptide model [24,77–79]. In a recent discrete dynamics study employing a novel coarse-grained force field PRIME20, several pathways of $A\beta_{17-42}$ aggregation from disordered oligomers to protofilaments have been identified, including U-shaped, O-shaped and S-shaped "seeds" [80]. However, application of discrete dynamics was shown to strongly enhance hydrogen bonding in proteins, resulting in overestimated β-content in comparison to fully atomistic MD [62]. Other works apply implicit solvent coarse grained model with optimized potential for efficient structure prediction (OPEP) force field, when backbone is described in all-atom representation, and side-chains are represented by centroids with different van-der-Waals radii associated [81]. To speed up folding simulations high-temperature MD have also been employed [82,83]. Other strategies for enhanced sampling include replica exchange MD (REMD) [84], Hamiltonian temperature REMD [85], meta-dynamics [86] and bias-exchange meta-dynamics [87,88]. These methods allow accelerating sampling, study folding and aggregation and reducing the size of studied systems. However, this is achieved at the expense of lower resolution and strong dependence on the choice of force fields [89] raising questions of the reliability of the predictions employing accelerated MD sampling, considering the demonstrated importance of the force fields in MD simulations [56,90,91].

An alternative approach employs partially misfolded constructs as initial structures for all-atom explicit-water MD simulations. In the absence of reliable structural information of the oligomeric/seed state, the usage of existing Aβ peptide protofilaments allows addressing the dynamics of β-rich constructs directly without long simulations of the transition to such constructs. In particular, several published MD simulations [49,67,92–94] were using hydrogen/deuterium-exchange NMR-derived structure 2BEG of $A\beta_{17-42}$ pentamer or its individual chains [92] as the initial model. The model helped to investigate template induced conformational changes [93], stability of annular intermediates [94], or fibril elongation [95]. Broader aspects of template-assisted aggregation have been addressed in recent review articles [50,54,55] and references therein. A slight limitation of starting simulations from an experimentally derived fibril fragment structure is the focus on the existing in-register parallel β-sheet aggregates which usually do not disintegrate spontaneously, neither form alternative anti-parallel constructs during MD simulations. Nevertheless, extensive simulations of protofilament-derived constructs in explicit solvent provide valuable information on the stability of these structures, as well as allow predicting new rotated forms [96] which can be seen as potential candidates of Aβ seed structures. Recently new Aβ peptide structures were published, such as the octamer of D23N mutant $A\beta_{17-40}$ fragments [48], and $A\beta_{1-40}$ nonameric fibril fragment [97], and $A\beta_{1-42}$ peptide dimers with face-to-face packing [98]. Computational modeling studies employing these new constructs can be expected to provide further insights into the molecular dynamics of Aβ peptide aggregates. Various descriptors have been employed to analyze the fibril stability. These include, for example, the number of side-chain to side-chain hydrogen bonds, the volume packing fraction within fibril fragment, and the frustration index [99]; geometrical distance between the planes of the core and the side-chains in vertical and horizontal directions [100]; as well as stability landscapes employing the binding free energies with dipolar solvent model [101].

In this work, we report extensive fully atomistic MD simulations of several model systems composed of ten to twelve $A\beta_{17-42}$ peptides in water with the addition of Cu^{2+} and Fe^{2+} ions. We use multiple randomly positioned monomers from protofibfil model [92] for our initial constructs, and employ an explicit water model for the solvent. Oligomers from C-terminal fragment $A\beta_{17-42}$, also known as P3, which mainly contain hydrophobic residues, may be expected to drive the processes of aggregation and fibrillization [49,67]. They are found in diffuse deposits associated with AD [16,17,19] and known to be toxic [16,17,20]. Although it is clear that electrostatic interactions should be important for the process of aggregation of $A\beta_{17-42}$ fragments, the influence of such common charge-bearing compounds as metal ions has not been investigated yet in a MD simulation of the aggregation. Even though fragment $A\beta_{17-42}$ does not contain the main metal binding site, possible influence of transient coordination through carboxyl groups begs for a better understanding. We investigate the evolution of these multimeric systems starting from initially random orientations of the Aβ peptide chains, specifically focusing on the changes in their secondary structure content and interatomic contacts. To the best of our knowledge, this is the first report describing the evolution of large (containing more than 6 units) multimeric Aβ peptide systems from initially random orientations down to the formation of more compact oligomeric aggregates, as observed from all-atom MD simulations in explicit solvent. To analyze the dynamical stability of the various constructs, we employ a novel essential collective dynamics (ECD) method that our group has developed and applied to analyze a number of biomolecular systems [102–110].

Methods

Modeling structures

Our initial structures comprise randomly positioned monomeric Aβ peptide fragments $_{17}$LVFFAEDVGSNKGAIIGLMVGGVVIA$_{42}$. For these monomer units, we used the coordinates of chains A-E of N-terminally truncated $A\beta_{17-42}$ experimentally derived pentamer from PDB ID 2BEG [92,111], see Figure 1(a). To prepare the control monomer system, chain C from 2BEG.pdb was extracted from the complex, minimized in vacuum, solvated in single point charge extended (SPCE) water box, and counterions Na^+/Cl^- were added (see Table 1, system A1). Next, using Accelrys VS [112] and VMD [113] packages, we have built a system containing ten monomers out of two sets of monomeric $A\beta_{17-42}$ units from 2BEG.pdb by randomly rotating and shifting the units against each other with a minimal distance of 5 Å, so that none of the units were in contact with each other. Then we minimized these ten randomly positioned units system in vacuum and added solvent and counterions (see Table 1, system A2). The $A\beta_{17-42}$ decamer system was NPT simulated in a SPCE water box for 50 ns. In order to probe the formation of multiples of hexamers as seen in experiments [26,27], water molecules and ions were removed from the decamer system and two more monomer units were added, randomly rotated and distanced by at least 5 Å from the other units (see Table 1, system A3). The resulting dodecameric system was also minimized in vacuum, solvated in SPCE water box, and electro-neutralized. The sites bearing negative charges, predominantly exposed carboxylate groups of E22 and D23 of different chains, were identified in system A3 employing *Accelrys Discovery Studio Visualizer* [112], and Cu^{2+} or Fe^{2+} ions were added to these sites resulting in systems A4a, A5a, and A6a (Table 1). To collect statistics on systems dynamics, we run additional control simulations for each of the systems A4a, A5a, and A6a, as listed in Tables 1 and S1. The same starting coordinates of atoms and changed seed numbers when random-generating the initial Maxwell distributions of atom velocities were used in the additional simulations, which are labeled as "b", "c", and so on. In systems A5 and A6 all metal ions were positioned in negatively charged cavities. In system A4a and the corresponding controls two Cu^{2+} ions were positioned in negatively charged cavities, and the third Cu^{2+} ion was positioned outside at a distance of approximately 7 Å from the surface of the oligomer.

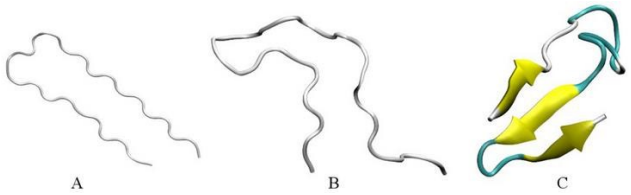

Figure 1: Snapshots of the secondary structure of $A\beta_{17-42}$ monomer (system A1) in 20 ns MD simulation: initial model before equilibration (A), random coil conformation at 12 ns (B), and three-fold conformation at 16 ns (C).

Table 1: The list of systems studied.

	System	Details of preparation
A1a, A1b	Aβ monomer	two systems, chains C and D from 2BEG.pdb [92]
A2	$A\beta_{17-42}$ (10) decamer, random chains position	based on 2BEG.pdb coordinates, monomers rotated by random angles and shifted by random distances of 5-7Å against each other
A3	$A\beta_{17-42}$ (12) dodecamer	based on A2 after 50 ns with two monomers added at random positions
A4a-A4e	$A\beta_{17-42}$ dodecamer with 3 Cu^{2+} ions	based on A3 with three Cu^{2+} ions added
A5a-A5e	$A\beta_{17-42}$ dodecamer with 6 Cu^{2+} ions	based on A3 with six Cu^{2+} ions added to negatively charged sites
A6a-A6e	$A\beta_{17-42}$ dodecamer with 6 Fe^{2+} ions	based on A3 with six Fe^{2+} ions added to negatively charged sites

All systems A4-A6 were minimized in vacuum, then water and Na^+/Cl^- counterions were added. Minimizations, equilibrations and production MD simulations on systems A1-A6 were carried out using Gromacs v4.5.3 package [114]. Optimized potentials for liquid simulations (OPLS) force fields [115] were used for the peptide molecules and ions. Subsequent solvent minimizations involved decreasing position restraints on non-hydrogen protein atoms, as well as and the heating with Berendsen thermostats and an NVT-equilibration.

Molecular dynamics simulations

The production MD simulations, and also the last equilibration step, were conducted at 310 K temperature and at a pressure of 1 atm with isotropic pressure coupling (NPT ensemble), and bond lengths restrained with the linear constant solver (LINCS) algorithm with a fourth order of expansion. These simulations were performed for 200 ns for systems A2, A3, A4a-e, A5a-e, and A6a-e (see Table S1). 1 fs time steps were used, and snapshots saved every 20 fs in order to analyze the essential collective dynamics. Additional details of system preparation and simulations have been described elsewhere [108].

Structural analysis of the trajectories, including assessment of secondary structure, calculations of RMSD, the number of hydrogen bonds and salt bridges, the radii of gyration, distance maps, and solvent accessible areas has been done using GROMACS package scripts [114] and the VMD package [113]. For graphical representation, the VMD and Accelrys VS packages were employed.

Essential collective dynamics (ECD)

The essential collective dynamics (ECD) method allows identifying persistent dynamic correlations in macromolecules from short fragments of MD simulation trajectories. According to the statistical-mechanical framework [102,107] macromolecular dynamics can be described by generalized Langevin equations (GLE) with essential collective coordinates defined by applying the principal component analysis (PCA) on MD trajectories. More specifically, short fragments of MD trajectories (usually from the last 20 ns of a production run) are analyzed. A fragment represents a temporal sequence of atomic positions,

$$\vec{q}_i(t) = \{x_i(t), y_i(t), z_i(t)\}, \quad i = 1,2,...,N, \tag{1}$$

where N is the number of atoms in the protein, and $x_i(t)$, $y_i(t)$, and $z_i(t)$ are Cartesian coordinates of atom i at discrete temporal snapshots denoted by the time variable t. From these data, a covariance matrix of size $3N \times 3N$ is calculated [102],

$$C_{ij} = < (\vec{q}_i(t) - < \vec{q}_i >)(\vec{q}_j(t) - < \vec{q}_j >) >, \tag{2}$$

where the averaging is done over all temporal snapshots in the fragment. In a multimer, the indices i,j in the covariance matrix (2) run over all atoms in all units. Eigenvectors and eigenvalues of the covariance matrix are obtained, and the eigenvectors ordered according to the magnitude of the corresponding eigenvalues. The complete set of $3N$ eigenvectors is then deduced to a lesser number of principal eigenvectors, which we also refer to as the essential collective coordinates [102],

$$\vec{E}^k = \{E_1^k, E_2^k, ...E_{3N}^k\}, \quad k = 1,2,...,K. \tag{3}$$

The number of principal eigenvectors K is selected such that 90% or more of the total displacements are sampled, which is usually achieved with K=10-30. The expression for the eigenvectors (3) can be equivalently rewritten as follows,

$$\vec{E}^k = \{\vec{r}_1^k, \vec{r}_2^k, ...\vec{r}_N^k\}, \quad k = 1,2,...,K. \tag{4}$$

Here $\vec{r}_i^k$ denote triplets of direction cosines $\{\vec{E}_{i,x}^k, \vec{E}_{i,y}^k, \vec{E}_{i,z}^k\}$ of eigenvectors $\vec{E}^k$ relative the x, y, and z degrees of freedom for atom $i = 1,2,...,N$ in $3N$-dimensional configuration space [102]. Equation (4) is equivalent to (3) with the only difference that $3N$ direction cosines defining each eigenvector are grouped into N triplets, such that each triplet is associated with one atom in the protein. It has been shown [102,107] that such triplets of direction cosines can be employed to evaluate dynamical coupling (correlation of motion) between atoms of the protein, to find out which of the atoms move coherently. For this purpose, a set of N vectors is constructed as follows [107]:

$$\vec{r}_i = \{\vec{r}_i^1, \vec{r}_i^2, ...\vec{r}_i^K\}, \quad i = 1,2,...,N. \tag{5}$$

Earlier it has been demonstrated that each of the vectors (5) identifies a projected image of the corresponding atom i in a $3K$-dimensional space[106] such that distances between the images of two atoms i and j,

$$d_{ij} = |\vec{r}_i - \vec{r}_j|, \quad i, j = 1,2,...,N, \tag{6}$$

represent the degree of dynamic correlation between these atoms [106,107]. In particular, short distances d_{ij} indicate that atoms i and j move coherently regardless of their proximity in 3D structure, whereas larger distances represent a relatively independent motion [106]. It has also been shown [107] that the values of d represent invariant (stable) correlations, and as such they allow predicting persistent dynamics trends from relatively short fragments of MD trajectories.

A suite of dynamics descriptors, such as the protein's dynamics domains [102]; main-chain flexibility profiles [103]; and main-chain/backbone and side-chain pair correlation maps [106,109] have been derived within the ECD framework, extensively validated, and successfully applied to analyze dynamics of proteins, protein-ligand, and protein-nanoparticle complexes [103–106,108–110]. Importantly, the ECD method does not require exhaustive sampling of the conformational space in order to draw accurate predictions. Short sub-nanosecond segments of MD trajectories are usually sufficient for a compatibility of the predictions with NMR experiments representing significantly longer time regimes [102,103,105–107].

In this work we assess the dynamics of Aβ aggregates using ECD dynamics domains, main-chain flexibility profiles, and backbone/side-chain correlation maps. The dynamics domains, which represent relatively rigid parts of the structure that move coherently, are identified through a clustering procedure described in detail in [102]. The ECD main chain flexibility descriptor $F_m^{C\alpha}$ for C_α atom in residue m is defined as a distance between the projected image of this C_α atom, $\vec{r}_m^{C\alpha}$, and the centroid over the images of all C_α atoms, $\vec{\varepsilon}^{C\alpha}$ [103]:

$$F_m^{C\alpha} = \left| \vec{r}_m^{C\alpha} - \vec{\varepsilon}^{C\alpha} \right|, \quad (7)$$

$$\vec{\varepsilon}^{C\alpha} = \frac{1}{N_{C\alpha}} \sum \vec{r}_m^{C\alpha} . \quad (8)$$

Index m in equations (7) and (8) runs over all residues in all chains of the Aβ aggregate. Finally, to calculate ECD main-chain correlation maps we use projected distances d_{ij} from equation (6), where indices *i* and *j* run over non-hydrogen, non-consecutive backbone atoms [106] in all chains of the aggregate. When calculating side-chain correlation maps, the indices run over non-hydrogen end-group atoms in all residues excluding glycines. More details of the calculations of ECD flexibility profiles and pair correlations can be found in our earlier reports [103–106] and [106,108–110], respectively. All ECD descriptors used in this work were obtained with K=20. For each construct considered, we employed 100 segments, each of 0.2 ns, from the last 20 ns of the MD trajectories, to obtain the averaged data for the analysis.

Table 2: Locations of stable β-strands in modeled Aβ systems. Indicated are residues that were populated for more than 26% of time during 20 ns simulation for system A1 and for more than 50% of time for 200 ns simulation for systems A2-A6.

Chain	System					
	A1	**A2**	**A3**	**A4a**	**A5a**	**A6a**
A	18-20, 33-35, 39-41	32-34	18-19, 31-34	29-34, 39-40	31-33	18-19, 29-32
B		18-20, 25-26, 34-37, 39-41	18-20, 25-26, 34-37, 39-41	18-19, 25-26, 34-41	18-20, 25-26, 35-37, 39-41	19-20, 37-40
C		32-33	32-33	18-19, 32-33	32-35	32-36
D		19-23, 31-36	18-22, 35-38	19-22, 31-36	19-20, 35-36	19-21, 34-36
E		18-21, 35-38	18-21	18-21, 39-40	18-21	18-22, 32-37
F		33-34	33-35	31-34	33-35	33-37
G		26-27, 31-32, 40-41	18-19,26-27, 31-32, 36-37,	26-27, 31-32, 40-41	26-27, 31-32, 40-41	26-27, 31-32
H		18-19, 28-29, 37-38	18-19, 37-38	18-19, 37-38	18-19	18-19, 37-38
I		39-41	18-20, 34-35, 39-41	18-20, 39-41	18-20, 39-41	
J		20-21, 32-34, 40-41	32-35	32-35, 37-38	32-35	32-35
K			34-35, 40-41	29-34	32-35	18-20, 36-39
L			34-35	32-39	34-37	19-24, 34-38

Results and Discussion

Multiple solvated $A\beta_{17-42}$ monomers form stable β-sheet containing oligomers.

Two independent 20 ns simulations of Aβ monomers (system A1) were conducted. As Figure 1 shows, individual solvated monomer units initially adopt a random-coil conformation without β-structure. In one of two trajectories for the monomer system, a three-fold anti-parallel β-sheet involving residues 18-20, 33-35, and 39-41 was detected during 26% of the simulation time (see Figure 1C and Table 2), consistent with the propensity of the $A\beta_{17-42}$ monomers to form β-sheets reported earlier [66]. However, for another monomer system we observed mainly random coils with a transient β-content present for only 2.3% of time. The formation of metastable β-strands close to C-terminus of Aβ monomers has been observed earlier in numerous modeling studies, such as for example [56,61,62,116,117].

In particular, β-sheet or β-hairpin motifs involving residues from regions 18-20, 30-32, and 39-41 have been observed [61,62,117]. Our finding of β-sheet locations (see Table 2 and Figure S2) is in good agreement with these studies. Some modeling works also report a significant α-helical content, especially in N-terminal region of Aβ monomers [61,62,118]. That we do not observe α-helices in this work, may be attributed to the absence of N-terminal region in $A\beta_{17-42,}$ and forcefileds used [56].

Figures 2A and 2B illustrate the structure of system A2, composed of ten randomly positioned $A\beta_{17-42}$ monomers in water, before and after the 200 ns MD simulation, respectively. As it is evident from Figure 2A, no β-structures were present in any of the chains initially. However, the decamer started aggregating already during the 0.2 ns NPT equilibration stage. This involved a rapid decrease of inter-chain separations and development of numerous side-chain contacts for the first 20-40 ns. Since the $A\beta_{17-42}$ peptide comprises mostly hydrophobic residues, the aggregation was accompanied by expulsion of water molecules from the inter-chain space within 40 ns of the simulation. The distance maps in Figure S1 show the mean smallest distances between side-

chain atoms (above the diagonal) and main-chain atoms (below the diagonal). As one can see from Figures S1A-S1C, about 80% of the closest inter-atomic contacts that we observe at 200 ns have been developed over the first 60 ns of the simulation. Further contact formation was relatively slow. As one could expect, somewhat shorter distances are observed between side-chain atoms in comparison to the main chain. Figure 3A shows the time dependence of the gyration radius of the decamer A2; Figure S2(B) shows the secondary structure evolution; Table 2 lists stable β-strands identified during 200 ns of the simulation; and the third row in Table 3 summarizes the various structural changes observed for this system. Overall in the course of a 200 ns simulation of the decamer, the radius of gyration has decreased from 30.66 Å to 20.82 Å, and a compact oligomer formed that contained both parallel and anti-parallel β-sheets. Often, although not always, stable β-strands are found in regions 18-21 and 31-41, where the monomeric system A1 also developed β-content during a 20 ns simulation (Figures 1C and S2, and Table 2). Overall, as Table 3 shows, β-content of system A2 increased from 3.7% to 20% in the course of 100 ns, and then decreased to 12.8% after 200 ns. This is accompanied by a pronounced increase in the number of inter-peptide and intra-peptide hydrogen bonds (HBs), as Figure 3B illustrates. During the first 100 ns of the molecular dynamics run, the decamer A2 developed 27 pairs of HBs, in addition to the existing 14 pairs of HBs which were already formed during the equilibration. However, during the next 100 ns the decamer lost some of these HBs, so that 36 bonds remained by end of the 200 ns simulation (see Table 3 and Figure 3B). We attribute this to a redistribution of hydrogen bonding with the solvent during the simulations. System A2 also developed 18 salt bridges (SBs) involving acidic residues E22 or D23 and basic residue K28 in the course of 200 ns of simulations.

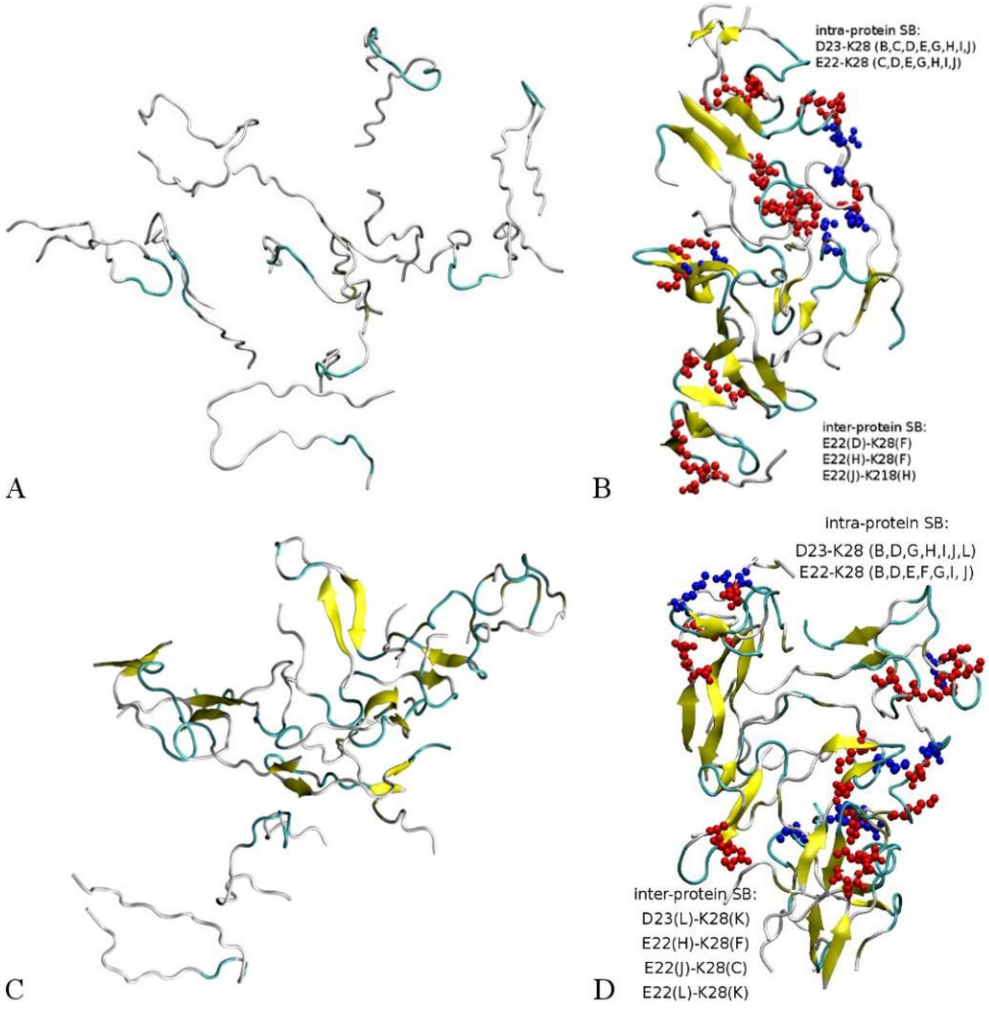

Figure 2: Ten $A\beta_{17-42}$ monomers in water (system A2) before MD simulation (A) and decamer formed after 200 ns of the simulations (B); $A\beta_{17-42}$ decamer after 50 ns of MD simulation with the addition of two monomers (system A3) before MD simulation (C) and dodecamer formed after 200 ns of the simulations (D). Random coils are indicated with white color, β-strands are shown by yellow and turns are shown by green. On panels B and D, inter-protein salt bridges (blue spheres) and intra-protein SB's (red spheres) are shown.

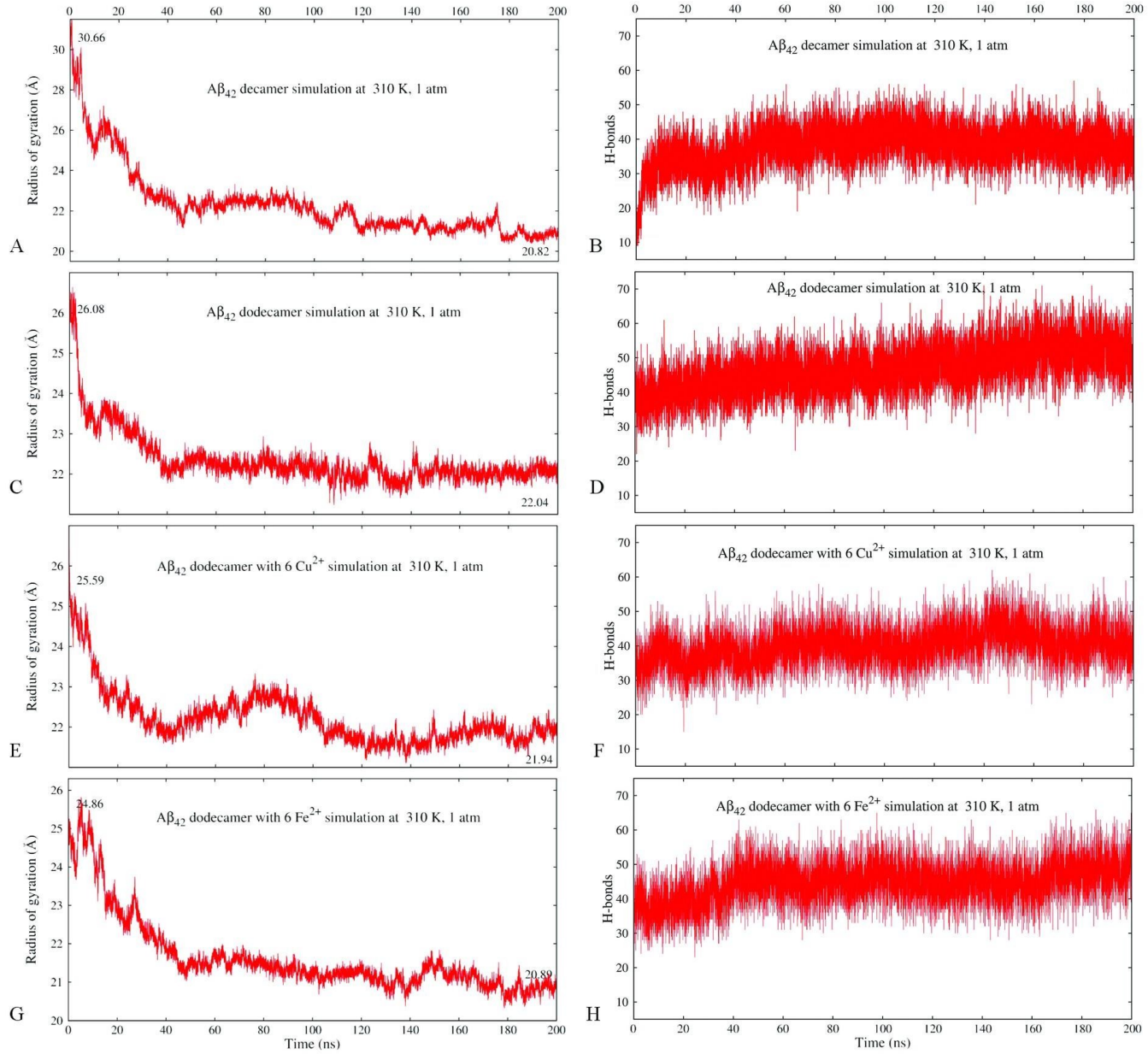

Figure 3: Changes in radius of gyration (protein's level of compactness) calculated by VMD over the simulation time (panels A,C,E,G) and detected number of hydrogen bond pairs (panels B,D,F,H) for systems A2 (A,B), A3 (C,D), A5a (E,F), and A6a (G,H).

Table 3: Changes in the number of HBs, SBs, secondary structure content, and gyration radius for different constructs in the beginning of the trajectory for 0 ns (the first number), after 100 ns (the second number) and after 200 ns (the third number).

		Hydrogen Bonds	Salt Bridges	α helical content, %	β-sheet content, %	Isolated bridges content %	Radius of gyration, Å
A2	10-mer	14-41-36	18	0-0-0%	3.7-20.0-12.8%	2.2-3.7-5.7%	30.66-21.76-20.82
A3	12-mer	39-47-50	18	0-0-0%	12.6-15.6-19.4%	5.6-7.1-7.4%	26.08-22.13-22.05
A4a	12-mer 3 Cu ions	36-45-51	16	0-0-0%	14.3-17.5-23.3%	5.0-4.0-4.1%	28.39-21.71-21.48
A5a	12-mer + 6 Cu ions	35-40-41	19	0-0.03-0.2%	14.5-15.9-13.3%	4.6-6.5-6.5%	25.59-22.28-21.94
A6a	12-mer + 6 Fe ions	38-46-51	13	0-0-0%	9.9-20.0-19.7%	6.5-4.6-5.2%	24.86-21.22-20.89

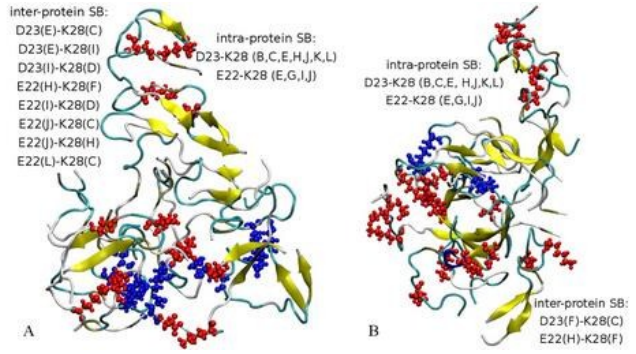

Figure 4: Intra-molecular and inter-molecular salt bridges (SB) for $A\beta_{42}$ dodecamers A5 with six Cu^{2+} ions (A) and A6 with six Fe^{2+} ions (B). The residues participating in intra-molecular SBs are indicated with red spheres, while residues in inter-molecular SBs are shown in blue.

Dodecamer systems A3-A6 were built by adding two $A\beta_{17-42}$ monomers to decamer system A2 after 50 ns of the simulation. As an example, Figure 2C shows the initial configuration of dodecameric system A3. Figures 2D, 4A, and 4B illustrate the structures of systems A3, A5a, and A6a respectively after 200 ns, and Figures 3C-3H show the evolution of the gyration radii and HB numbers.

Since the initial structures for dodecamers A3-A6 were composed of a partially aggregated decamer with two additional chains distanced by more than 5 Å, the initial sizes of systems A3-A6 were slightly higher than the size of system A2, whereas the number of initial HBs in these systems was equal to the final number of HBs in system A2 after 50 ns (see Table 3). Similarly to system A2, the dodecamer systems A3-A6 have decreased in size, developed hydrogen bonds and maintained salt bridge networks during the simulations. Remarkably, the β-sheet content increased in most cases in comparison to the initial composite structure. The locations where stable β-content is found involve residues 18-21 and 31-41, similarly as for the decamer (Table 2). The dodecamer structures were formed from decamers after 50 ns of simulations, when 37 HBs were present. After 200 ns of simulations, the number of hydrogen bonds increased reaching the total of 41-51 bonds. However, no significant change in the number of salt bridges was observed in dodecamers A3 and A5a. Interestingly, dodecamer A5a with six Cu^{2+} ions developed one SB more than dodecamer A3 without ions, but less HBs and less β-sheet content; whereas dodecamer A6a with six Fe^{2+} ions exhibited less SBs than A3, but showed an almost similar number of HBs and similar β-sheet content (see Table 3 and Figure 4). Overall, acidic residues E22, D23 and basic residue K28 were often involved in inter-molecular or intra-molecular salt bridges for all Aβ systems, although in the system A6a with six Fe^{2+} ions some of the bridges were disrupted.

Peptide aggregation involves rapid collapse and slow relaxation stages.

As mentioned in the previous section, a rapid decrease in inter-chain separation in Aβ oligomers has been observed during the first 20-60 ns of the MD simulations, followed by longer, slower structural changes. The corresponding time dependencies for the radius of gyration for $A\beta_{17-42}$ decamer (A2) and dodecamer (A3) shown in Figures 3A and 3C, respectively, exhibit two distinct phases. A quick collapse of the decamer occurs within the first 40 ns, followed by a slower relaxation afterwards. The dependence of the number of hydrogen bonds on time for decamer A2 depicted in Figure 3B exhibits a quick increase followed by a slower trend to saturation, compatible with the described two-stage process of aggregation, however a slight decrease follows after approximately 100 ns. In contrast, the dependence of the number of HBs in dodecamer A3 shows a smooth increase with time throughout the entire 200 ns simulation (Figure 3D). Figures S3 (A,C) compare the evolution of the radius of gyration of systems A5a (A) and A6a (C) with the corresponding control simulations, which exhibit similar trends, although one can see some variations of the gyration radius for the systems.

All systems studied show significant fluctuations of the radius of gyration typical for MD (see Figures 3 and S3). In dodecamers A5 and A6 with six Cu^{2+} or Fe^{2+} ions the fluctuations are especially pronounced. Unlike the other systems, dodecamer A5a with six Cu^{2+} ions exhibits wave-like expansions and contractions (Figure 3E) accompanied by well-discernible waves in the number of HBs. The average number of HBs in system A5a after 200 ns is lower than in system A3 (Figure 3F). When six Fe^{2+} ions are added to Aβ dodecamer instead of Cu^{2+} ions, the resulting system A6a develops a similar number of HBs as dodecamer A3 without ions. It also shows a milder expansion-contraction variation of the gyration radius than system A5a. Figures S3 (B,D) compare the HB numbers of systems A5a (B) and A6a (D) with the control simulations. The resulting amounts of HBs built would be approximately the same in all simulations for both systems.

Figure S4 shows typical solvent-accessible surface representation of systems A3a, A5a, and A6a at 70 ns and at 200 ns. The control systems A5 and A6 (not shown) exhibit similar trends as in Figures S4 (B-E). While systems without ions and those with copper ions develop more compact, oval-like shapes, systems with iron ions tend to form more developed surfaces. Since in initial constructs Aβ monomers were placed at a distance from each other, all oligomers initially contained cavities and channels formed by connecting of two or more peptide chains. However, most of the channels have disappeared completely or transformed into cavities in the course of the relaxation stage, or approximately 30-40 ns. By 70 ns and thereafter, only a few cavities are found in A5 and A6 systems.

Overall, radius of gyration of the initial quasi decameric system A2 of 30.66 Å decreased to 20.82 Å after 200 ns (Figure 3A),

whereas an initially more compact dodecamer A3 decreased its gyration radius from 26.08 Å down to 22.05 Å (Figure 3C). Dodecamer with six Fe^{2+} ions A6a developed an even more compact structure (20.89 Å) than the dodecamer with six Cu^{2+} ions A5a (21.94 Å) as Figures 3E and 3G illustrate. In dodecamers A3, A5a, and A6a, the radius of gyration has largely stabilized after 80-120 ns, however their hydrogen bonding systems continued to develop throughout the entire 200 ns simulations (Figures 3D, 3F, and 3H).

Cu^{2+} and Fe^{2+} ions develop coordination bonds with negatively charged groups of $A\beta_{17-42}$

Detailed close-up images of copper/iron ions in systems A5a, and A6a are shown on Figures 5A-D and S5. In all the systems we observe transient coordination bonds of the ions with carboxylate groups E22, D23, and A42 via electrostatic interaction in aqueous environment. In systems A5a and A6a, as well as in the corresponding controls, all six ions were positioned in negatively charged cavities, all of which happened to be close to at least one acidic side-chain E22. These ions started forming coordination bonds with neighbor carboxylate groups immediately during equilibrations. In system A5a and the corresponding controls six copper ions initially developed bonds with carboxylate groups of E22 in negative charged cavities of the oligomer. In the course of production simulations the initial bonding of each copper ion to at least one E22 group was preserved, and additional bonds with groups from the same or other chains were formed. For example, Cu^{2+} ion shown in Figure 5A developed a bond to carboxylate group of E22 from chain A in system 5Aa after equilibration.

As Figure 5B shows, after 200 ns of production simulations this ion remained bound to E22 of chain A, and additionally developed a bond to C-terminal carboxyl group of A42 of chain J. An example of different Cu^{2+} ion from system A5a is illustrated in Figures S5A and S5B. This ion was initially bound to E22 of chain C in close proximity to E22 of chain L (Figure S5A), whereas after 200 ns simulations it additionally bounded to A42 from chains L and E, while remaining bound to E22 of chain C (Figure S5B). Fe^{2+} ions in system A6a and the corresponding controls A6b and A6c exhibit a similar coordination pattern. After equilibration they were mainly bound to carboxylate groups of E22. Most of the ions remained in the same bonding position during the entire production run. However, as the oligomers aggregated and become more compact, slight re-arrangements of the coordination occurred in most cases. As Figures S5C and S5D illustrate, a Fe^{2+} ion from system 6Aa has retained its initial coordination bonding to E22 of chain F and D23 of chain H., However, amide group of hydrophobic residue I31 of chain L has moved closer to the ion by end of the 200 ns simulation, and formed a van der Waals bond. In the example shown in Figures 5C and 5D, a Fe^{2+} ion that was initially in contact with E22 of chain C and with E22 of chain L, has been approached by amide group of I32 from chain I during the simulations, and developed a close van der Waals bond. Overall, in both systems A5 and A6 the majority of metal coordination bonds were formed with carboxylate groups of E22, D23 and C-terminal carboxyl group of A42, often from different chains. After 200 ns of production simulations, six Cu^{2+} ions in system A5a had the total of 14 such bonds, and six Fe^{2+} ions in system A6a had 13 bonds. Out of these, 7 bonds Cu^{2+} ions and 8 bonds of Fe^{2+} ions were with E22. Overall, bonds with E22 occur roughly twice as often as bonds with D23 or A42 each. We did not observe any substantial differences between Cu^{2+} and Fe^{2+} coordination bonding to $A\beta_{17-42}$ oligomers.

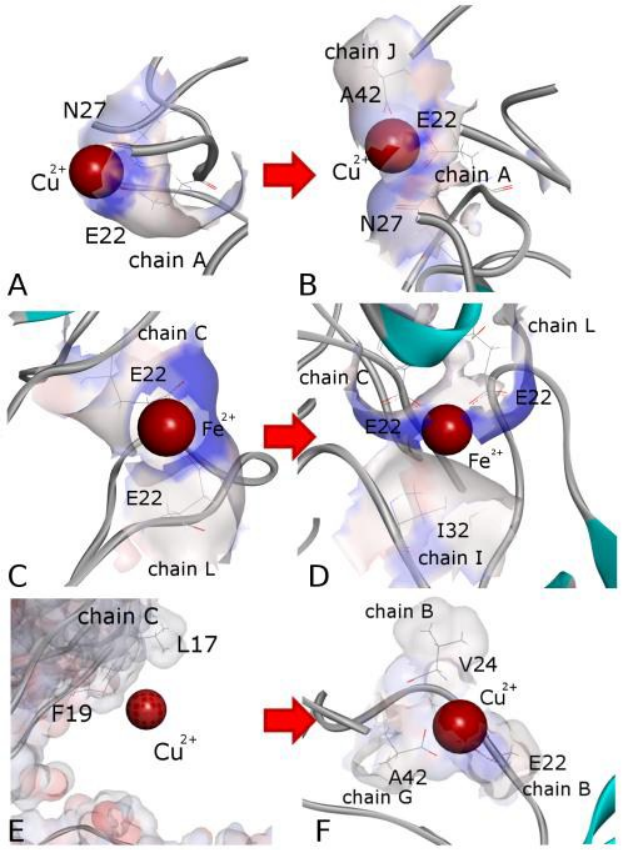

Figure 5: Close-up images of metal ions in systems A5a (A,B), A6a (C,D), and A4a (E,F) after equilibration (A,C,E) and after 200 ns (B,D,F). The ions shown in panels (A-D) were initially placed in negatively charged cavities.

A similar behaviour was also observed for two Cu^{2+} ions positioned in negatively charged cavities in system A4a (see Figures S6E-S6F) as well as in the corresponding controls. The third Cu^{2+} ion, which was positioned at a distance from the surface of chain C in oligomer A4a (Figure 5E), has traveled along the periphery of the oligomer until it developed a coordination bond with carboxyl group of C-terminal residue A42 of chain G after the first 10 ns of production simulation. This bond remained stable for the subsequent 190 ns of the simulation, and another bond with E22 of chain B was also established, resulting in the ion remaining positioned between chains B and G (Figure 5E) at a distance of approximately 37 Å from its initial location. In three out of four similar control systems, Cu^{2+} ions positioned distantly also developed coordination bonds, yet at different locations. In first and third

control systems A4b and A4d the ion has bound to E22 of chain A at a distance of 28-29 Å from its initial location, and in fourth system A4e the ion has bound to A42 of chains G and F at a distance of 32 Å from its initial location. In second control system, A4c, the ion did not bound to any group of the oligomer, and remained in solution. We attribute the relocations of these ions primarily to random-walk occurring until they develop a coordination bond with a negatively charged group.

Remarkably, in our simulations all metal ions have developed coordination bonds with multiple residues of the $A\beta_{17-42}$ oligomers, and retained most of these bonds in the absence of the N-terminal metal binding cite. Furthermore, we observe a coordination of the ions by similar groups, especially E22, which was found to move into the coordination sphere of Cu^{2+} when it is bound in the N-terminal site of $A\beta_{1-42}$ monomer [76]. Also, consistent with published simulations [76], we do not observe a coordination of metal ions by M35.

ECD analysis of Aβ oligomers reveals strong impact of secondary and tertiary structures on the dynamics

The essential collective dynamics analysis (ECD) has been performed on the modelled systems employing trajectory fragments from the last 20 ns of simulations. The essential collective dynamics theory employs a set of principal eigenvectors of the covariance matrix to describe correlations between pairs of atoms in the system. The number of the eigenvectors required to sample the total displacement with a given accuracy (principal components) defines the essential dimensionality of the system. Figure S7 shows a dependence of the percentage of the total displacement sampled by the principal components as a function of the number of the components, in average over a hundred of 0.2 ns long segments of MD trajectories for systems A2-A6. It can be seen that 20 principal components sample more than 97% of the displacement for all the systems.

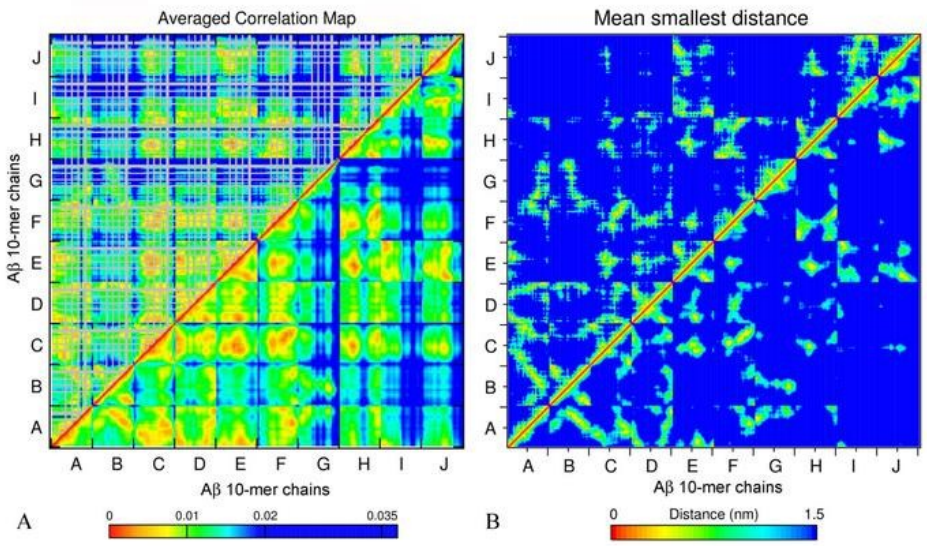

Figure 6: Side chain (above the diagonal) and backbone (below the diagonal) ECD correlation map (A) and mean smallest distance map calculated with the GROMACS software (B) for decamer A2. In the correlation maps, stronger correlations are shown by red, orange, and yellow colors, and weaker correlations are shown with blue color. In the side-chain correlation maps, glycine residues are excluded (shown in grey color) because of absent side chain. The distance maps show mean smallest distances between main-chain (below the diagonal) and side-chain (above the diagonal) atoms. In the distance maps, shorter distances are shown with red, orange, and yellow colors, and longer distances are shown in blue.

We used 20 principal eigenvectors to determine ECD correlations of motion between main-chain and side-chain atoms (see Methods) in the systems considered. Figure 6A shows the side-chain (above the diagonal) and backbone (below the diagonal) correlations in decamer A2 averaged over 100 0.2 ns long segments from 180-200 ns of the simulation, and Figure 6B shows the corresponding mean distances for comparison (the colors were intentionally selected to match the correlation maps). The comparison of side-chain and main-chain correlations indicates a pronounced similarity. In most cases, stronger correlations of side-chains are found in regions where backbone correlations are also stronger. As the correlation map indicates, units A-F, H, and most of N-ter of units I and J have formed a coherently moving sub-aggregate. The areas of strongest pair correlations (colored in red and orange) often include stable β-sheet formations. In particular hydrophobic residues V18-A21, which are often implicated in β-sheets, tend to exhibit strong inter-unit correlations. In turn, strong correlations can also be seen between units that are located close to each other according to the distance map, for example units F and H. Units G and C-ter of units I and J exhibit the weakest correlations with the rest of the oligomer. According to Table 2 and Figure S2, unit I of system A2 also forms little β-structure, and according to Figure 2B, this unit does not form inter-chain salt bridges. Contrarily, units G and J form three stable β-strands each. However in the weakly

correlated units, β-sheets are located within the units, rather than across different units. Unit G also does not exhibit inter-chain salt bridges (Figure 2B). In units B, D, E, G, H, K, and L, an "X"-shaped pattern of intra-chain correlations is visible, which is related to antiparallel hairpin-like bending of these units.

From comparison of the pair correlation map with the distance maps for system A2 (Figures 6A and 6B) it is evident that residues located in close proximity of each other also tend to develop strong correlations, as one could expect. However, Figure 6A also shows strong correlations between some of the residues positioned distantly from each other, such as for example, units B and C, or units J and A. This can be explained by non-direct interactions between the residues mediated by water or other residues, which, in turn, allows those residues to move coherently.

Pair correlations and mean smallest distance maps of dodecamer A3 (Figure S8) show similar trends as for decamer A2. As described in Methods, the dodecamer was obtained by adding two units to A2. These added units, denoted as K and L in Figure S8, formed close contacts and strong correlations with units E, I and J. Strong dynamical coupling in sub-aggregate composed of units A-F, H, I and J is observed in the dodecamer similarly to system A2. Some of the correlations, especially involving units I and J, have increased and new correlations, primarily with unit L, have formed extending the strongly correlated sub-aggregate.

In order to visualize the strongest correlations in the oligomers more explicitly, we have identified the largest coherently moving domains within the same ECD framework (see Methods). Figure 7 depicts major dynamics domains in decamer A2 as well as in dodecamers A3 and A5a mapped onto the corresponding tertiary structures. For each of the oligomers, the largest dynamic domain is shown in blue color. As one can see from the figure, in the three systems the largest domain of correlated motion occupies the central part of the oligomer, whereas smaller domains and off-domain parts are located primarily in the peripheral regions. The domain colored blue is clearly the largest in dodecamer A3, where the domain also contains more β-structures than in the other two systems. For the dodecamer with six copper ions A5a, the second and third largest domains (colored in red and green, respectively) involve more residues than in two systems without ions. For system A5a, the largest domain is slightly smaller than in two other systems.

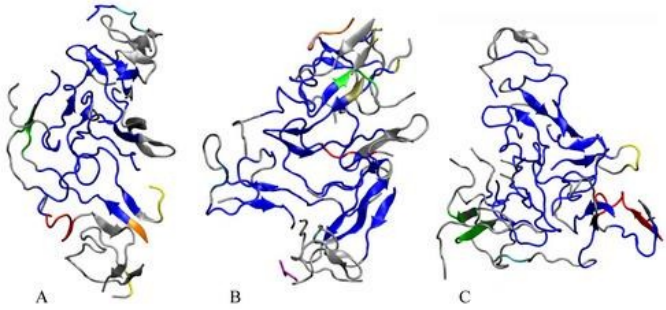

Figure 7: Dynamics domains of correlated motion in Aβ decamer A2 (A), dodecamer A3 (B) and dodecamer with six Cu^{2+} ions A5a (C). The dynamics domains, representing the most rigid parts of the oligomers, are colored blue, red, green, yellow, cyan, orange, pink, light blue, purple, tan, and mauve in order of decreasing size of the domains. Off-domain regions are shown in gray.

The ECD flexibility profiles of dodecamers A3, A5a, and A6a are presented on Figure 8. Since in these systems unit L is located in closest proximity with units two other units K and J, its flexibility is somewhat lower than that of unit K. Overall, units D, G, H and K are positioned on the periphery of the oligomer, and therefore most of them show a relatively high flexibility. In contrast, units A, B, C, E and F are located in the central part of the oligomer, and they show a relatively low flexibility in all three systems. In systems A5a and A6a that contain ions, the flexibilities of units B, C, F, and L are somewhat lower in areas where an ion was located, but other regions may have an increased flexibility.

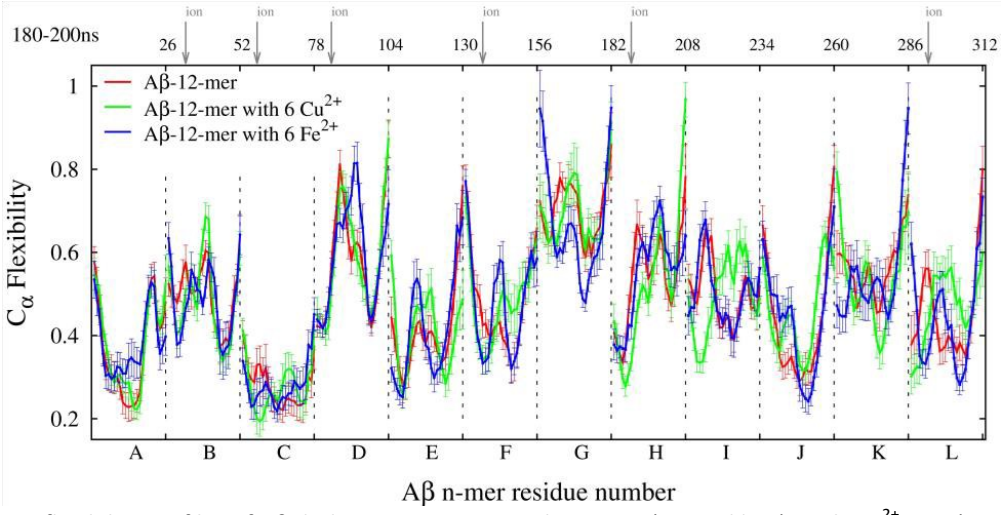

Figure 8: Main chain flexibility profiles of Aβ dodecamer systems without ions (A3, red line), with Cu^{2+} ions (A5a, green line), and with Fe^{2+} ions (A6a, blue line). The letters along the lower axis denote the chains, and the vertical arrows on top indicate where Cu^{2+} or Fe^{2+} ions were positioned in dodecamers A5a and A6a, respectively.

In globular proteins with stable secondary structure, high levels of the ECD flexibility descriptor usually correspond to flexible loops as well as termini, whereas most of the flexibility minima indicate α-helices or β-sheets[103–106,108]. Consistent with this, Figure 8 shows an increase in main-chain flexibility at terminal regions of the twelve units. Comparison of positions of the main-chain flexibility minima in Figure 8 with the positions of stable β-strands in Table 2 reveals a significant, although not a complete overlap. As it can be seen from Table 2 and Figure S2, system A3 exhibits the total of 24 stable β-strands, and systems A5a and A6a develop 19 stable β-strands each. Out of these, 15 β-strands in systems A3 and A6a each, and 14 β-strands in system A5a are located in immediate proximity of main-chain flexibility minima. In particular, β-strands located in regions 18-21 and 31-37 are often associated with minima of flexibility. For example, a minimum around residue 19 of unit H in all three systems indicates a β-strand, which also affects the flexibility of adjacent units F and J, which are in direct contact with it. However, not all stable β-strands could be associated with flexibility minima. For nine β-strands in A3, seven β-strands in A5a, and three β-strands in A6a, no proximal flexibility minima were identified. We attribute this to occasional increase in overall mobility of the short peptide chains, such as for example for several β-strands in positions 39-41 close to C-termini. In turn, not all of main-chain flexibility minima seen in Figure 8 could be associated with stable β-structures. In particular, some of such flexibility minima are found at positions 23-24 and 29-31 adjacent to residues 22, 23, and 28 that are often involved in salt bridges. The formation of salt bridges seems to be accompanied by a buildup of steric constrains on the neighboring residues, which explains the observed decrease in flexibility.

Figure 9 presents ECD pair correlation maps (panels A, C,) and distance maps (panels B, D) of Aβ oligomers A5a and A6a averaged over 100 segments of the last 20 ns (180-200 ns) of the corresponding trajectories. The correlation maps show both side-chain correlations (above the diagonal) and backbone correlations (below the diagonal). Similarly to decamer A2 and dodecamer A3, stronger correlations of side-chains are found in regions where backbone correlations are also stronger.

Figures 9B and 9D represent averaged distance maps over the set of conformations for the time interval of 180-200 ns. As in systems A2 and A3, the strongest pair correlations shown in red and orange colors in Figures 9A and 9C have a lot in common with the corresponding contact distance maps, however distant correlations are also observed. This implicates that residues in immediate proximity tend to move coherently in many cases, although mediated indirect interactions are also present.

For both dodecamers with the ions added, strong inter-chain correlations involving units A-F are evident from Figures 9A and 9C, similarly as observed in systems A2 and A3. .Units H, I, J, and L exhibit strong inter-chain correlations with C, E, and F in both systems, however these correlations tend to be stronger in dodecamer A6a with Fe ions than in dodecamer A5a with Cu ions (Figures 9A, 9C). In both dodecamers, unit G exhibits low correlations with the rest of the oligomer (Figures 9A and 9B) consistent with its relatively high flexibility (Figure 8). In the MD trajectories, this chain was also found the weakest bound. When compared with the ion-free dodecameric system A3 (Figure S8), systems A5a and A6a exhibit buildup of close intern-chain contacts of several units. In both ion-containing systems, unit C developed more contacts with K and H, as chains K and H shifted towards an ion around chain C; unit D in turn developed more contacts with E; and the latter additionally developed more contacts with H and I (Figures 9B, 9D, and S8B). With the exception of contacts of C with K and E with I in system A5a, this buildup of additional contacts was accompanied by an increase in corresponding inter-chain correlations shown in Figures 9A, 9C, and S8A. At the same time, both systems A5a and A6a exhibit an increase in correlations of unit H with F and K in the absence of a pronounced increase in their contacts. In both ion-containing systems, units C and H exhibit the most extensive increase of inter-chain contacts or correlations, especially with E, F, K, and L. The peripheral chain L, however, lost both in contacts and correlations with units E, I, J, and K upon addition of the ions. Another notable loss in correlation in comparison to system A3 occurred between units J in E in both A5a and A6a dodecamers. However, overall increase in inter-chain contacts and/or in correlations prevails over the losses. Most chains that have shown changes in the dynamics in comparison with ion-free dodecamer, either were in close proximity of initial ion positions (such as units C and H), or developed coordination bonds with ions during simulations (for example F, E, and L). The inter-chain correlation data suggest that presence of the ions may promote shifts of neighbouring chains closer towards ion locations, tending to increase inter-chain dynamical coupling.

Similarly to the case of systems A2 and A3, in dodecamers A5a and A6a units A-F and H are strongly inter-correlated. Significant parts of units I, J, K. and L also show pronounced inter-chain correlations. The regions that tend to be β-populated are also often associated with stronger intra-chain and inter-chain correlations in the oligomers. For example in A5a, residues 30-35 of unit K which accommodate a stable β-strand, exhibit pronounced inter-chain correlations with C, F, H, and L. In particular, strong correlations are observed between residues 33-40 of unit K and residues 30-38 of unit L (Figure 9A), where β-sheets were found (Table 2 and Figure S2). In A6a, β-populated regions of unit K also show strong correlations with other units. A similar tendency is also clearly seen in unit L for both systems A5a and A6a. Strong correlations of unit A with units F and J were found for A6a, while for A5a the correlations are less pronounced. Correlation maps also show strong correlations for mostly hydrophobic residues L34-A41 and F19-A21, which are often β-populated.

Overall, from comparison of Figures 6A, S8, 9A, and 9C it is evident that the dodecamers exhibit more pronounced inter-chain correlations than observed in decamer A2.

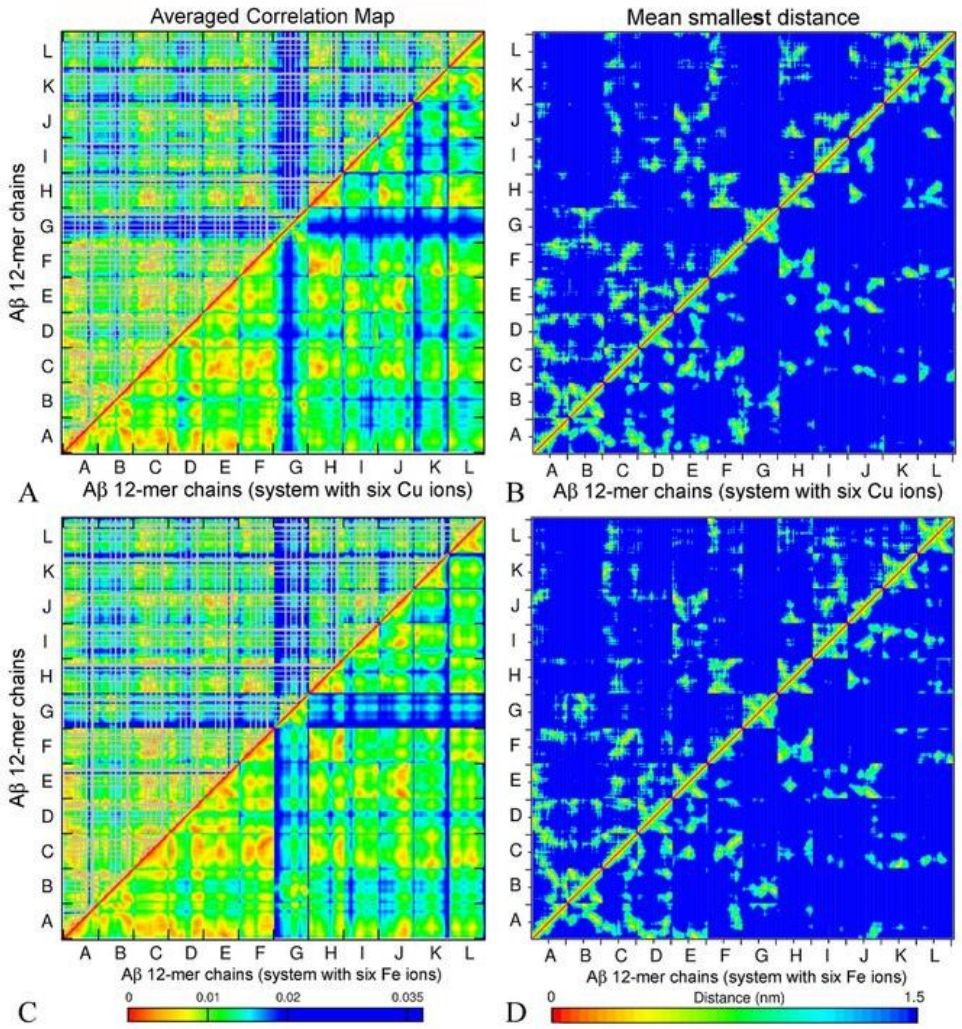

Figure 9: Side chain (above the diagonal) and backbone (below the diagonal) ECD correlation maps (A, C), and mean smallest distance maps calculated with the GROMACS software (B, D) for dodecamer A5a (A, B) and dodecamer A6a (C, D). The color schemes are as in Figure 6.

Hydrophobic and hydrophilic interactions influence oligomer's stability and morphology

The results discussed above indicate that hydrophobic and electrostatic interactions are strongly implicated in the oligomer formation. To characterize these interactions, we have calculated changes in total solvent-accessible surface area (SASA) of hydrophobic and hydrophilic groups in decamer A2, dodecamer A3 without ions, and dodecamer A4a with three Cu ions along 200ns MD trajectories. In the case of $A\beta_{17-42}$ peptide, hydrophilic groups involve N- and C-terminal charged atoms, asparagine, aspartic acid, glutamic acid, lysine, and serine. The remaining 16 residues are considered hydrophobic. The normalized per-atom SASA for hydrophobic and hydrophilic groups are depicted in Figures 10A and 10B, respectively. The figures show that both hydrophobic and hydrophilic exposures have decreased in the course of simulations in all there constructs. In decamer A2 SASA of hydrophilic groups was slightly higher at the beginning of the simulation, and after 200 ns it decreased less than the SASA of hydrophobic groups. This is consistent with the general trend for hydrophilic groups to remain exposed to the solvent, and for hydrophobic groups to become buried. Since decamer A2 was initially less compact than the dodecamers, the initial SASA of system A2 is higher than for A3 and A4a. However, at the end of the 200 ns simulation, the SASA for all the three systems has stabilized at the same level in average. In dodecamers A3 and A4a, the fraction of hydrophobic exposed area is slightly lower than that in decamer A2 until 180 ns of the simulation, after which the exposures adopt similar values. A significant portion of the hydrophobic exposure, approximately 57%, is due to valine and isoleucine residues (Figure S9). For example, a slight increase in hydrophobic side-chain SASA for dodecamer A4a over the last 20 ns of the simulation was caused by the exposure of isoleucines and phenylalanines.

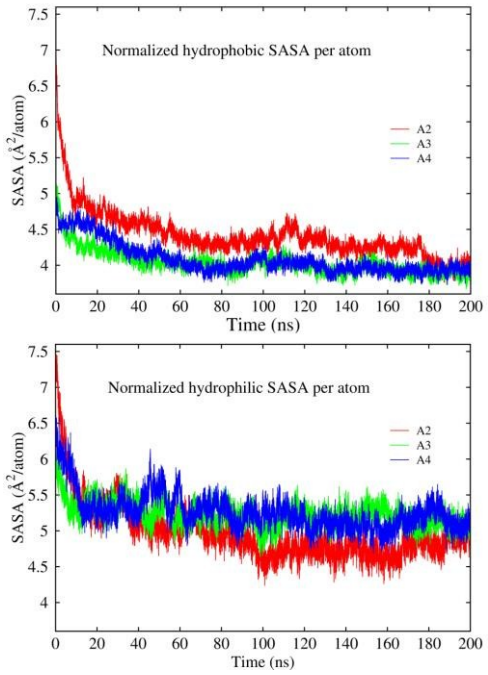

Figure 10: Normalized solvent accessible surface area of hydrophobic (A) and hydrophilic (B) groups in decamer A2 (red line) and dodecamers A3 and A4a (green and blue lines) over the course of 200 ns MD simulations.

Figure 11 demonstrates the conformation for dodecamer A4a with three Cu^{2+} ions after 195.5 ns of the simulation. After approximately 30 ns of production run, due to connection of chains one channel has formed in central region in close proximity of copper ion bound to E22 of chain C, and another channel has formed in a peripheral region. The channels' widths varied subsequently. By end of 200 ns run, the dodecamer has adopted an asymmetrical doughnut-like shape with a large channel in the central part and a smaller one in the peripheral region as Figure 11 shows. According to Table 3, β-content in this dodecamer is higher than in other systems considered. One can see from the Figure 11 that locations of channels in the structure are coinciding with the positions of copper ions. This suggests that copper ions may compete with development of salt bridges and other bonds in the oligomer, thereby creating favorable conditions for the development of channels in the oligomers. In distinction from the other dodecamers, in A4a unit G is better correlated with the rest of the oligomer, while unit D and the central part of unit H are less correlated, as the correlation map in Figure S10 shows. All chains are well-intertwined together: unit C (dark grey color on Figure 11A) is located in the central part of the oligomer, and is covered with unit A (blue), which in turn is overlapped by unit B (red). Unit H (green) is connected to units A, F (brown) and G (light grey). Unit J (pink) is in contact with unit C (dark grey) and unit L (purple), which in turn is in contact with unit K (cyan). Unit I (white) is bound to unit E, and in turn to unit J. Unit D (orange) is located between units A and E (yellow) and has the smallest inter-chain interaction area, as well as the largest solvent exposure.

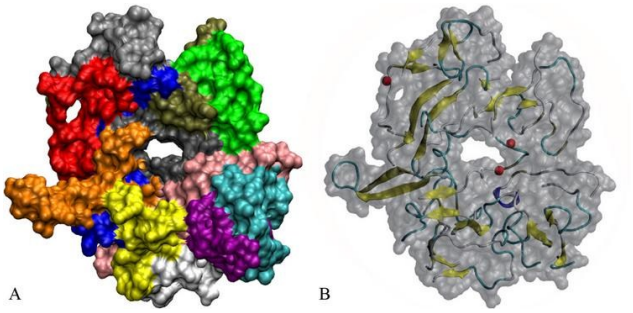

Figure 11: Doughnut-like conformation of $A\beta_{17-42}$ dodecamer A4a with three copper ions added at 195.5 ns. A– solvent accessible surface representation with twelve units shown with different colors; B - translucent solvent accessible surface with the secondary structure and location of three copper ions shown.

Control systems A4b, A4c, and A4d have developed less symmetrical yet compact, slab-like oligomers with channels or cavities in similar locations as in A4a (Figure S11). In both systems a cavity or channel was close to two of the ions, which positions were also similar across the systems 4a. However, the channels are narrower than in system A4a at similar simulation times. Overall, the described evolution of solvent accessible surfaces suggests that coordination bonds of metal ions may affects the oligomer compactness at the slow relaxation stage. As the chains slowly change their position, cavities and holes tend to form in close proximity to the ion location.

Conclusions

Molecular dynamics simulations reported in this work indicate that $A\beta_{17-42}$ peptides tend to form compact oligomers in aquatic environment. Consistent with recent experimental findings [29], our modeling results suggest that aggregation of 10-12 Aβ monomers tends to produce stable globular-like, largely unstructured oligomers without a pronounced long-range alignment of the units. After 200 ns of the simulations, the oligomers exhibited 13% – 23% of β-sheet content. Stable β-strands were often found in regions 18-21 and 31-41 of the peptide chains, which is compatible with full-length simulations of Aβ monomers [62]. Both parallel and anti-parallel β-sheets were observed.

Two stages of the oligomer formation have been identified in the course of the 200 ns MD simulations, quick collapse within the first 40 ns, and slow relaxation afterwards. The collapse stage is characterized by quick decrease of inter-chain separation, disappearance of most cavities and channels, development of numerous inter-chain contacts, and buildup of the β-sheet content. Formation of hydrogen bonds and salt bridges, and expulsion of water from inter-chain space followed by burial of hydrophobic side chains appear to be the main driving forces of the first stage. The subsequent relaxation stage involves a slow decrease of the gyration

radius. In the decamer system, this was accompanied by a partial decrease in β-sheet content.

The essential collective dynamics analysis of the Aβ oligomers indicates that motion of some units is inter-correlated stronger than others. Coherently moving sub-aggregates of 6-9 units have been detected, most of which are located in the central part of the oligomers. This agrees with the size of oligomers seen in experiments on $A\beta_{1-42}$ aggregation in-vitro, which have been hypothesized to be building blocks for larger toxic complexes [119]. Although strong inter-chain correlations were often found in the vicinity of stable β-sheets, this was not always the case. Chains located close to each other in the tertiary structure were often found to move coherently in the absence of stable β-content. Main-chain flexibility of the oligomers exhibited similar trends as in globular proteins [103,105,106,108]. This includes increased flexibility at terminal regions of the units, and minima of the flexibility in the vicinity of stable β-strands and salt bridges.

Coordination bonding of Cu^{2+} and Fe^{2+} ions involving carboxylate groups of E22, D23 and A42 was found for all simulated oligomers. Once formed, the coordination bonds have remained stable during our simulations. The Cu^{2+} and Fe^{2+} bonding does not prevent $A\beta_{17-42}$ from forming compact non-fibrillary oligomers, indicating that disruption of $A\beta_{1-42}$ fibrils formation seen in experiments [44] involves different mechanisms than observed at early stages of $A\beta_{17-42}$ aggregation. Presence of Cu^{2+} and Fe^{2+} ions in negatively charged cavities of dodecameric oligomers was often found to result in decreased main-chain flexibility in the areas close to the ions, as well as in stronger inter-chain correlations. In the case of Fe^{2+} ions, this was accompanied by a slightly less compact oligomer with stronger inter-chain dynamical correlations. In one of trajectories for the oligomer with six Cu^{2+} ions added, pronounced wave-like expansion and contraction of the oligomer was observed at the slow relaxation stage, accompanied by a variation in the number of hydrogen bonds. Dramatic changes were observed in the dodecamer containing three Cu^{2+} ions. This dodecamer has repeatedly developed channels or cavities across several control simulations. In one simulation, this aggregate adopted a doughnut-like shape with a large channel in the central part and a smaller one in a peripheral region. Both channels were located close to a Cu^{2+} ion, suggesting that the ions might compete for development of bonds in the oligomer, thereby facilitating the formation of channels.

Acknowledgements

The authors thank Johnathan Mane, John Mohan, Nataraj Pagadala, Oliver Stueker, Bilkiss Issack, Taras Fito, Mark Berjanskii, and Nikolay Blinov for their programming contributions and stimulating discussions. Molecular images were created using VMD package [113] and Discovery Studio Visualizer v4.0 [112]. Simulations were carried using NINT-NRC computational cluster and WestGrid and Compute Canada resources. Support of the work by Alberta Prion Research Institute is gratefully acknowledged (APRI Project 201300006).

Notes and references

1 M. Bucciantini, E. Giannoni, F. Chiti, F. Baroni, L. Formigli, J. Zurdo, N. Taddei, G. Ramponi, C. M. Dobson and M. Stefani, *Nature*, 2002, **416**, 507–511.
2 B. Caughey and P. T. Lansbury, *Annu. Rev. Neurosci.*, 2003, **26**, 267–298.
3 J. A. Hardy and G. A. Higgins, *Science*, 1992, **256**, 184–185.
4 S. Baglioni, F. Casamenti, M. Bucciantini, L. M. Luheshi, N. Taddei, F. Chiti, C. M. Dobson and M. Stefani, *J. Neurosci.*, 2006, **26**, 8160–8167.
5 I. Benilova, E. Karran and B. De Strooper, *Nat. Neurosci.*, 2012, **15**, 349–357.
6 J. Hardy and D. J. Selkoe, *Science*, 2002, **297**, 353–356.
7 R. Kayed, E. Head, J. L. Thompson, T. M. McIntire, S. C. Milton, C. W. Cotman and C. G. Glabe, *Science*, 2003, **300**, 486–489.
8 C. A. McLean, R. A. Cherny, F. W. Fraser, S. J. Fuller, M. J. Smith, K. Beyreuther, A. I. Bush and C. L. Masters, *Ann. Neurol.*, 1999, **46**, 860–866.
9 T. L. Williams, B. R. G. Johnson, B. Urbanc, A. T. A. Jenkins, S. D. A. Connell and L. C. Serpell, *Biochem. J.*, 2011, **439**, 67–77.
10 L. Jiang, C. Liu, D. Leibly, M. Landau, M. Zhao, M. P. Hughes and D. S. Eisenberg, *eLife*, 2013, **2**, e00857.
11 R. J. Castellani, H. Lee, S. L. Siedlak, A. Nunomura, T. Hayashi, M. Nakamura, X. Zhu, G. Perry and M. A. Smith, *J. Alzheimers Dis. JAD*, 2009, **18**, 447–452.
12 A. L. Lublin and S. Gandy, *Mt. Sinai J. Med. N. Y.*, 2010, **77**, 43–49.
13 Y. Fezoui and D. B. Teplow, *J. Biol. Chem.*, 2002, **277**, 36948–36954.
14 C. Wu and J.-E. Shea, *PLoS Comput. Biol.*, 2013, **9**.
15 A. Jan, D. M. Hartley and H. A. Lashuel, *Nat. Protoc.*, 2010, **5**, 1186–1209.
16 A. M. Szczepanik, D. Rampe and G. E. Ringheim, *J. Neurochem.*, 2001, **77**, 304–317.
17 W. Wei, D. D. Norton, X. Wang and J. W. Kusiak, *Brain*, 2002, **125**, 2036–2043.
18 E. Gowing, A. E. Roher, A. S. Woods, R. J. Cotter, M. Chaney, S. P. Little and M. J. Ball, *J. Biol. Chem.*, 1994, **269**, 10987–10990.
19 L. S. Higgins, G. M. Murphy, L. S. Forno, R. Catalano and B. Cordell, *Am. J. Pathol.*, 1996, **149**, 585–596.
20 R. L. Patton, W. M. Kalback, C. L. Esh, T. A. Kokjohn, G. D. Van Vickle, D. C. Luehrs, Y.-M. Kuo, J. Lopez, D. Brune, I. Ferrer, E. Masliah, A. J. Newel, T. G. Beach, E. M. Castaño and A. E. Roher, *Am. J. Pathol.*, 2006, **169**, 1048–1063.
21 T. Pillot, M. Goethals, B. Vanloo, C. Talussot, R. Brasseur, J. Vandekerckhove, M. Rosseneu and L. Lins, *J. Biol. Chem.*, 1996, **271**, 28757–28765.
22 M. Bibl, M. Gallus, V. Welge, S. Lehmann, K. Sparbier, H. Esselmann and J. Wiltfang, *Proteomics Clin. Appl.*, 2012, **6**, 163–169.
23 L.-F. Lue, Y.-M. Kuo, A. E. Roher, L. Brachova, Y. Shen, L. Sue, T. Beach, J. H. Kurth, R. E. Rydel and J. Rogers, *Am. J. Pathol.*, 1999, **155**, 853–862.
24 B. Urbanc, L. Cruz, S. Yun, S. V. Buldyrev, G. Bitan, D. B. Teplow and H. E. Stanley, *Proc. Natl. Acad. Sci. U. S. A.*, 2004, **101**, 17345–17350.

25 K. Pauwels, T. L. Williams, K. L. Morris, W. Jonckheere, A. Vandersteen, G. Kelly, J. Schymkowitz, F. Rousseau, A. Pastore, L. C. Serpell and K. Broersen, *J. Biol. Chem.*, 2012, **287**, 5650–5660.
26 S. L. Bernstein, N. F. Dupuis, N. D. Lazo, T. Wyttenbach, M. M. Condron, G. Bitan, D. B. Teplow, J.-E. Shea, B. T. Ruotolo, C. V. Robinson and M. T. Bowers, *Nat. Chem.*, 2009, **1**, 326–331.
27 G. Bitan, M. D. Kirkitadze, A. Lomakin, S. S. Vollers, G. B. Benedek and D. B. Teplow, *Proc. Natl. Acad. Sci.*, 2003, **100**, 330–335.
28 G. P. Gellermann, H. Byrnes, A. Striebinger, K. Ullrich, R. Mueller, H. Hillen and S. Barghorn, *Neurobiol. Dis.*, 2008, **30**, 212–220.
29 J. Luo, S. K. T. S. Wärmländer, A. Gräslund and J. P. Abrahams, *Biochemistry (Mosc.)*, 2014, **53**, 6302–6308.
30 N. J. Economou, M. J. Giammona, T. D. Do, X. Zheng, D. B. Teplow, S. K. Buratto and M. T. Bowers, *J. Am. Chem. Soc.*, 2016.
31 T. D. Do, N. E. LaPointe, R. Nelson, P. Krotee, E. Y. Hayden, B. Ulrich, S. Quan, S. C. Feinstein, D. B. Teplow, D. Eisenberg, J.-E. Shea and M. T. Bowers, *J. Am. Chem. Soc.*, 2015.
32 M. P. Lambert, A. K. Barlow, B. A. Chromy, C. Edwards, R. Freed, M. Liosatos, T. E. Morgan, I. Rozovsky, B. Trommer, K. L. Viola, P. Wals, C. Zhang, C. E. Finch, G. A. Krafft and W. L. Klein, *Proc. Natl. Acad. Sci. U. S. A.*, 1998, **95**, 6448–6453.
33 A. I. Bush, *Trends Neurosci.*, 2003, **26**, 207–214.
34 J. Dong, C. S. Atwood, V. E. Anderson, S. L. Siedlak, M. A. Smith, G. Perry and P. R. Carey, *Biochemistry (Mosc.)*, 2003, **42**, 2768–2773.
35 L. M. Sayre, G. Perry, P. L. Harris, Y. Liu, K. A. Schubert and M. A. Smith, *J. Neurochem.*, 2000, **74**, 270–279.
36 L. Hou and M. G. Zagorski, *J. Am. Chem. Soc.*, 2006, **128**, 9260–9261.
37 C. Hureau, Y. Coppel, P. Dorlet, P. L. Solari, S. Sayen, E. Guillon, L. Sabater and P. Faller, *Angew. Chem. Int. Ed.*, 2009, **48**, 9522–9525.
38 T. Miura, K. Suzuki, N. Kohata and H. Takeuchi, *Biochemistry (Mosc.)*, 2000, **39**, 7024–7031.
39 C. S. Atwood, R. C. Scarpa, X. Huang, R. D. Moir, W. D. Jones, D. P. Fairlie, R. E. Tanzi and A. I. Bush, *J. Neurochem.*, 2000, **75**, 1219–1233.
40 V. A. Streltsov, S. J. Titmuss, V. C. Epa, K. J. Barnham, C. L. Masters and J. N. Varghese, *Biophys. J.*, 2008, **95**, 3447–3456.
41 Y. Miller, B. Ma and R. Nussinov, *Coord. Chem. Rev.*, 2012, **256**, 2245–2252.
42 J. Danielsson, R. Pierattelli, L. Banci and A. Gräslund, *FEBS J.*, 2007, **274**, 46–59.
43 D. Drago, S. Bolognin and P. Zatta, *Curr. Alzheimer Res.*, 2008, **5**, 500–507.
44 M. Mold, L. Ouro-Gnao, B. M. Wieckowski and C. Exley, *Sci. Rep.*, 2013, **3**, 1256.
45 M. Innocenti, E. Salvietti, M. Guidotti, A. Casini, S. Bellandi, M. L. Foresti, C. Gabbiani, A. Pozzi, P. Zatta and L. Messori, *J. Alzheimers Dis. JAD*, 2010, **19**, 1323–1329.
46 K. Suzuki, T. Miura and H. Takeuchi, *Biochem. Biophys. Res. Commun.*, 2001, **285**, 991–996.
47 B. Moores, E. Drolle, S. J. Attwood, J. Simons and Z. Leonenko, *PLoS ONE*, 2011, **6**, e25954.
48 W. Qiang, W.-M. Yau, Y. Luo, M. P. Mattson and R. Tycko, *Proc. Natl. Acad. Sci. U. S. A.*, 2012, **109**, 4443–4448.
49 G. Reddy, J. E. Straub and D. Thirumalai, *Proc. Natl. Acad. Sci. U. S. A.*, 2009, **106**, 11948–11953.
50 J.-E. Shea and B. Urbanc, *Curr. Top. Med. Chem.*, 2012, **12**, 2596–2610.
51 E. Gazit, *FASEB J. Off. Publ. Fed. Am. Soc. Exp. Biol.*, 2002, **16**, 77–83.
52 A. W. P. Fitzpatrick, G. M. Vanacore and A. H. Zewail, *Proc. Natl. Acad. Sci.*, 2015, 201502214.
53 N. G. Franco R, *J. Neurol. Neurol. Disord.*, 2014, **1**, 103.
54 G. Wei, N. Mousseau and P. Derreumaux, *Prion*, 2007, **1**, 3–8.
55 A. Morriss-Andrews and J.-E. Shea, *Annu. Rev. Phys. Chem.*, 2015, **66**, 643–666.
56 L. Tran and T. Ha-Duong, *Peptides*, 2015, **69**, 86–91.
57 J. Nasica-Labouze, P. H. Nguyen, F. Sterpone, O. Berthoumieu, N.-V. Buchete, S. Coté, A. De Simone, A. J. Doig, P. Faller, A. Garcia, A. Laio, M. S. Li, S. Melchionna, N. Mousseau, Y. Mu, A. Paravastu, S. Pasquali, D. J. Rosenman, B. Strodel, B. Tarus, J. H. Viles, T. Zhang, C. Wang and P. Derreumaux, *Chem. Rev.*, 2015, **115**, 3518–3563.
58 M. Yang and D. B. Teplow, *J. Mol. Biol.*, 2008, **384**, 450–464.
59 M. Ito, J. Johansson, R. Strömberg and L. Nilsson, *PLOS ONE*, 2011, **6**, e17587.
60 Y.-S. Lin, G. R. Bowman, K. A. Beauchamp and V. S. Pande, *Biophys. J.*, 2012, **102**, 315–324.
61 N. G. Sgourakis, Y. Yan, S. McCallum, C. Wang and A. E. Garcia, *J. Mol. Biol.*, 2007, **368**, 1448–1457.
62 B. Barz and B. Urbanc, *PLoS ONE*, 2012, **7**, e34345.
63 D. J. Rosenman, C. Wang and A. E. García, *J. Phys. Chem. B*, 2016, **120**, 259–277.
64 A. Huet and P. Derreumaux, *Biophys. J.*, 2006, **91**, 3829–3840.
65 B. Tarus, J. E. Straub and D. Thirumalai, *J. Mol. Biol.*, 2005, **345**, 1141–1156.
66 B. Urbanc, L. Cruz, F. Ding, D. Sammond, S. D. Khare, S. V. Buldyrev, H. E. Stanley and N. V. Dokholyan, *Biophys. J.*, 2004, **87**, 2310–2321.
67 N. Blinov, L. Dorosh, D. Wishart and A. Kovalenko, *Biophys. J.*, 2010, **98**, 282–296.
68 N.-V. Buchete, R. Tycko and G. Hummer, *J. Mol. Biol.*, 2005, **353**, 804–821.
69 N.-V. Buchete and G. Hummer, *Biophys. J.*, 2007, **92**, 3032–3039.
70 A. Kahler, H. Sticht and A. H. C. Horn, *PLoS ONE*, 2013, **8**.
71 D. Thirumalai, G. Reddy and J. E. Straub, *Acc. Chem. Res.*, 2012, **45**, 83–92.
72 J. J. Valle-Delgado, M. Alfonso-Prieto, N. S. de Groot, S. Ventura, J. Samitier, C. Rovira and X. Fernàndez-Busquets, *FASEB J. Off. Publ. Fed. Am. Soc. Exp. Biol.*, 2010, **24**, 4250–4261.
73 S. L. Gallion, *PLoS ONE*, 2012, **7**, e49375.
74 H. Jang, F. T. Arce, S. Ramachandran, R. Capone, R. Azimova, B. L. Kagan, R. Nussinov and R. Lal, *Proc. Natl. Acad. Sci.*, 2010, **107**, 6538–6543.
75 W. Li, J. Zhang, Y. Su, J. Wang, M. Qin and W. Wang, *J. Phys. Chem. B*, 2007, **111**, 13814–13821.
76 D. F. Raffa and A. Rauk, *J. Phys. Chem. B*, 2007, **111**, 3789–3799.
77 J. M. Borreguero, B. Urbanc, N. D. Lazo, S. V. Buldyrev, D. B. Teplow and H. E. Stanley, *Proc. Natl. Acad. Sci.*, 2005, **102**, 6015–6020.
78 S. Yun, B. Urbanc, L. Cruz, G. Bitan, D. B. Teplow and H. E. Stanley, *Biophys. J.*, 2007, **92**, 4064–4077.
79 B. Urbanc, M. Betnel, L. Cruz, G. Bitan and D. B. Teplow, *J. Am. Chem. Soc.*, 2010, **132**, 4266–4280.

80 M. Cheon, C. K. Hall and I. Chang, *PLoS Comput. Biol.*, 2015, **11**, e1004258.
81 S. Santini, N. Mousseau and P. Derreumaux, *J. Am. Chem. Soc.*, 2004, **126**, 11509–11516.
82 N. Ferguson, R. Day, C. M. Johnson, M. D. Allen, V. Daggett and A. R. Fersht, *J. Mol. Biol.*, 2005, **347**, 855–870.
83 A. R. Lam Ng, *PhD Thesis*, 2008, 80.
84 A. Baumketner and J.-E. Shea, *J. Mol. Biol.*, 2007, **366**, 275–285.
85 R. Laghaei, N. Mousseau and G. Wei, *J. Phys. Chem. B*, 2011, **115**, 3146–3154.
86 A. Barducci, M. Bonomi, M. K. Prakash and M. Parrinello, *Proc. Natl. Acad. Sci. U. S. A.*, 2013, **110**, E4708–E4713.
87 L. E. Buchanan, E. B. Dunkelberger, H. Q. Tran, P.-N. Cheng, C.-C. Chiu, P. Cao, D. P. Raleigh, J. J. de Pablo, J. S. Nowick and M. T. Zanni, *Proc. Natl. Acad. Sci.*, 2013, **110**, 19285–19290.
88 S. Piana and A. Laio, *J. Phys. Chem. B*, 2007, **111**, 4553–4559.
89 P. H. Nguyen, M. S. Li and P. Derreumaux, *Phys. Chem. Chem. Phys. PCCP*, 2011, **13**, 9778–9788.
90 W. M. Berhanu, F. Yaşar and U. H. E. Hansmann, *ACS Chem. Neurosci.*, 2013, **4**, 1488–1500.
91 J. A. Lemkul and D. R. Bevan, *J. Phys. Chem. B*, 2010, **114**, 1652–1660.
92 T. Lührs, C. Ritter, M. Adrian, D. Riek-Loher, B. Bohrmann, H. Döbeli, D. Schubert and R. Riek, *Proc. Natl. Acad. Sci. U. S. A.*, 2005, **102**, 17342–17347.
93 W. Xi, W. Li and W. Wang, *J. Phys. Chem. B*, 2012, **116**, 7398–7405.
94 J. Zheng, H. Jang, B. Ma and R. Nussinov, *J. Phys. Chem. B*, 2008, **112**, 6856–6865.
95 W. Han and K. Schulten, *J. Am. Chem. Soc.*, 2014, **136**, 12450–12460.
96 A. De Simone and P. Derreumaux, *J. Chem. Phys.*, 2010, **132**, 165103.
97 J.-X. Lu, W. Qiang, W.-M. Yau, C. D. Schwieters, S. C. Meredith and R. Tycko, *Cell*, 2013, **154**, 1257–1268.
98 M. Schmidt, A. Rohou, K. Lasker, J. K. Yadav, C. Schiene-Fischer, M. Fändrich and N. Grigorieff, *Proc. Natl. Acad. Sci.*, 2015, **112**, 11858–11863.
99 J. H. Choi, C. Govaerts, B. C. H. May and F. E. Cohen, *Proteins*, 2008, **73**, 150–160.
100 Q. Van Vuong, Z. Bednarikova, A. Antosova, P. D. Q. Huy, K. Siposova, N. A. Tuan, M. S. Li and Z. Gazova, *Med Chem Commun*, 2015.
101 M. R. Smaoui, F. Poitevin, M. Delarue, P. Koehl, H. Orland and J. Waldispühl, *Biophys. J.*, 2013, **104**, 683–693.
102 M. Stepanova, *Phys. Rev. E Stat. Nonlin. Soft Matter Phys.*, 2007, **76**, 051918.
103 N. Blinov, M. Berjanskii, D. S. Wishart and M. Stepanova, *Biochemistry (Mosc.)*, 2009, **48**, 1488–1497.
104 K. Barakat, B. B. Issack, M. Stepanova and J. Tuszynski, *PLoS ONE*, 2011, **6**, e27651.
105 K. P. Santo, M. Berjanskii, D. S. Wishart and M. Stepanova, *Prion*, 2011, **5**, 188–200.
106 B. B. Issack, M. Berjanskii, D. S. Wishart and M. Stepanova, *Proteins Struct. Funct. Bioinforma.*, 2012, **80**, 1847–1865.
107 A. Potapov and M. Stepanova, *Phys. Rev. E*, 2012, **85**, 020901(R).
108 L. Dorosh, O. A. Kharenko, N. Rajagopalan, M. C. Loewen and M. Stepanova, *PLoS Comput Biol*, 2013, **9**, e1003114.
109 O. Stueker, V. A. Ortega, G. G. Goss and M. Stepanova, *Small Weinh. Bergstr. Ger.*, 2014, **10**, 2006–2021.
110 L. Dorosh, N. Rajagopalan, M. C. Loewen and M. Stepanova, *FEBS Open Bio*, 2014, **4**, 496–509.
111 F. C. Bernstein, T. F. Koetzle, G. J. Williams, E. F. Meyer, M. D. Brice, J. R. Rodgers, O. Kennard, T. Shimanouchi and M. Tasumi, *Eur. J. Biochem. FEBS*, 1977, **80**, 319–324.
112 *Accelrys Discovery Studio Visualiser*, BIOVIA.
113 W. Humphrey, A. Dalke and K. Schulten, *J. Mol. Graph.*, 1996, **14**, 33–38.
114 H. J. C. Berendsen, D. van der Spoel and R. van Drunen, *Comput. Phys. Commun.*, 1995, **91**, 43–56.
115 W. L. Jorgensen, D. S. Maxwell and J. Tirado-Rives, *J. Am. Chem. Soc.*, 1996, **118**, 11225–11236.
116 C. Wu, M. M. Murray, S. L. Bernstein, M. M. Condron, G. Bitan, J.-E. Shea and M. T. Bowers, *J. Mol. Biol.*, 2009, **387**, 492–501.
117 S. Côté, P. Derreumaux and N. Mousseau, *J. Chem. Theory Comput.*, 2011, **7**, 2584–2592.
118 S. Kim, T. Takeda and D. K. Klimov, *Biophys. J.*, 2010, **99**, 1949–1958.
119 I. A. Mastrangelo, M. Ahmed, T. Sato, W. Liu, C. Wang, P. Hough and S. O. Smith, *J. Mol. Biol.*, 2006, **358**, 106–119.